Doctor thesis

Experimental Study on Mass and Momentum Transfer Characteristics in 90° Elbow

（90°エルボ内の物質と運動量輸送に関する実験的研究）

March, 2019

Yuya Ikarashi

Doctoral program in Advanced Materials Science and Technology

Graduate School of Science and Technology

Niigata University

Doctor of engineering (2019) Niigata University
(Mechanical engineering)

TITLE	:	Experimental Study on Mass and Momentum Transfer Characteristics in 90° Elbow
Author	:	Yuya Ikarashi
Supervisor(s)	:	Professor Nobuyuki Fujisawa
Number of pages	:	97

Experimental Study on Mass and Momentum Transfer Characteristics in 90° Elbow

ABSTRACT

Mass and momentum transfer characteristics in and downstream of a 90° elbow are studied experimentally with the aid of the plaster dissolution method, surface flow visualization, and the particle image velocimetry (PIV) in and downstream of the elbow. The experiments are carried out for the elbow with the radius to diameter ratio 1.0, 1.2, and 1.5 in a Reynolds number Re = (3-15**)** × 10^4. The mass transfer measurements in the elbow indicate that the major change of mass transfer coefficient is observed along the inner wall of the elbow, where low mass transfer coefficient is found in the first half of the inner wall and it increases abruptly in the second half of the elbow, which is followed by a gradual recovery of the mass transfer in the downstream. However, the mass transfer on other wall does not change so much with that of the straight pipe. These features are mainly due to the flow acceleration in the first half of the inner wall and the following flow separation in the second half of the inner wall, where the high turbulence energy production is found in the PIV measurement. These results indicate that the mass transfer coefficient in and downstream of the elbow is highly modified by the flow separation in the elbow, which generates high turbulence energy in the second half of the inner wall in the elbow. Furthermore, these flow phenomena are highly promoted by increasing the elbow curvature and magnify the mass transfer on the inner

wall of the elbow and they are function of the Reynolds number in the range of present experiments.

Table of Contents

	Title	・・・1
	Abstract	・・・1
	Table of contents	・・・3
	List of figures	・・・5
	Nomenclature	・・・8
Chapter 1	Introduction	・・・9
1.1	Background	・・・9
1.2	Purpose of this research	・・・16
	Reference	・・・18
Chapter 2	Mass and Momentum Transfer Characteristics of 90° long Elbow	・・・23
2.1	Introduction	・・・23
2.2.	Experimental apparatus and procedures	・・・23
2.2.1	Experimental set-up	・・・23
2.2.2	Test elbow for mass transfer measurement	・・・24
2.2.3	Measurement of mass transfer characteristics	・・・26
2.2.4	Surface flow visualization by oil film method	・・・28
2.2.5	Measurement of velocity field by SPIV	・・・29
2. 3.	Results and discussion	・・・30
2.3.1	Distributions of mass transfer coefficient on elbow	・・・30
2.3.2	Visualization of surface flow in elbow	・・・32
2.3.3	Distributions of mass transfer coefficient downstream of elbow	・・・34
2.3.4	Mean velocity and turbulence energy downstream of elbow	・・・35
2.3.5	Axial variation of mass transfer coefficient in and downstream of elbow	・・・38
2.4.	Conclusion	・・・41
	References	・・・42
Chapter 3	Influence of Elbow Curvature on Flow and Turbulence Structure	・・・45
3.1.	Introduction	・・・45
3.2.	Experimental Apparatus and Procedures	・・・45
3.2.1	Experimental setup	・・・45
3.2.2	Measurement of velocity field by PIV	・・・47
3.3.	Results and Discussion	・・・51
3.3.1	Mean flow characteristics in elbow	・・・51

3.3.2 Turbulence characteristics in an elbow ・・・57
3.3.3 Cross-sectional distribution of mean and turbulence character--istics near the elbow outlet ・・・62
3.3.4 POD analysis of flow structure near elbow outlet ・・・66
3.4. Conclusions ・・・68
Appendix A Image deformation correction and uncertainty ・・・69
Appendix B Mean and axial turbulence intensity contours upstream of elbow ・・・70
References ・・・72
Chapter 4 Mass transfer measurement and flow separation behavior in a 90° short elbow ・・・74
4.1 Introduction ・・・74
4.2. Experimental apparatus and procedures ・・・74
4.2.1 Experimental set-up ・・・74
4.2.2 Mass transfer measurement ・・・74
4.2.3 PIV measurement of velocity field on inner elbow wall ・・・78
4.2.4 Evaluation of separation and reattachment points by near-wall PIV measurement ・・・79
4.3. Results and discussion ・・・80
4.3.1 Distribution of mass transfer coefficients in short elbow ・・・80
4.3.2 PIV measurement of velocity field over separating flow region ・・・84
4.4. Conclusion ・・・91
References ・・・93
Chapter 5 Concluding Remarks ・・・95
Acknowledgements ・・・97

List of figures

Fig. 1.1 Pipe-line layout of Mihama nuclear power plant ・・・10

Fig. 1.2 Picture of pipe break at Mihama nuclear power plant ・・・10

Fig. 2.1 Schematic layout of water tunnel and test elbow ・・・24

Fig. 2.2 Design of test elbow for mass transfer measurement ・・・26

(a) Test elbow geometry, (b) Inner - outer and side walls

Fig. 2.3. Pictures of test elbow for mass transfer measurement ・・・26

(a)Inner wall, (b) Outer wall, (b) Side wall

Fig. 2.4 Experimental test section for mass transfer measurement ・・・28

Fig. 2.5 Experimental test section for velocity field measurement ・・・30

Fig. 2.6 Cross-sectional mass transfer distributions in elbow ・・・32

(a) α= 0°, (b) 22.5°, (c) 45°, (d) 67.5°, (e) 90°

Fig. 2.7 Surface flow visualization ・・・34

(a)Inner wall, (b) Outer wall, (b) Side wall

Fig. 2.8 Cross-sectional mass transfer distributions downstream of elbow ・・・35

(a)x/d=0.5, (b) x/d=1, (c) x/d=2, (d) x/d= 3

Fig. 2.9 Cross-sectional mean velocity contours downstream of elbow ・・・37

(a)x/d=0.5, (b) x/d=1, (c) x/d=2, (d) x/d= 3

Fig. 2.10 Cross-sectional distributions of turbulence energy downstream of elbow

(a)x/d=0.5, (b) x/d=1, (c) x/d=2, (d) x/d= 3 ・・・37

Fig. 2.11 Axial variation of mass transfer coefficients in and downstream of elbow

(a) Inner wall, (b) Outer wall, (c) Side wall ・・・39

Fig. 3.1 Experimental setup ・・・47

Fig. 3.2 Details of experimental test section ・・・47

(a)Top view, (b) View from downstream

Fig. 3.3 Experimental arrangement of stereo PIV system ・・・49

Fig. 3.4 Streamwise mean velocity distribution in and downstream of the elbow for three radius ratios ・・・54

Fig. 3.5 Wall-normal mean velocity distribution in and downstream of the elbow for three radius ratios ・・・55

Fig. 3.6 Streamwise mean velocity distribution in and downstream of the elbow for three Reynolds numbers ・・・56

Fig. 3.7 Wall-normal mean velocity distribution in and downstream of the elbow for three Reynolds numbers ・・・57

Fig. 3.8 Axial turbulence intensity distribution in and downstream of the elbow for three radius ratios ・・・59

Fig. 3.9 Wall-normal turbulence intensity distribution in and downstream of the elbow for three radius ratios ・・・59

Fig. 3.10 Reynolds stress distribution in and downstream of the elbow for three radius ratios ・・・60

Fig. 3.11 Axial turbulence intensity distribution in and downstream of elbow for three Reynolds numbers ・・・61

Fig. 3.12 Normal turbulence intensity distribution in and downstream of the elbow for three Reynolds numbers ・・・62

Fig. 3.13 Reynolds stress distribution in and downstream of the elbow for three Reynolds numbers ・・・62

Fig. 3.14 Cross-sectional velocity field near the elbow outlet. (a) r/d = 1.0, (b) r/d = 1.2, (c) r/d = 1.5 ・・・63

Fig. 3.15 Mean velocity contours near the elbow outlet (x/d = 0.5) (a) r/d = 1.0, (b) r/d = 1.2, (c) r/d = 1.5 ・・・65

Fig. 3.16 In-plane velocity magnitude contours near the elbow outlet (x/d = 0.5) (a) r/d = 1.0, (b) r/d = 1.2, (c) r/d = 1.5 ・・・65

Fig. 3.17 Axial turbulence intensity contours near the elbow outlet (x/d = 0.5) (a) r/d = 1.0, (b) r/d = 1.2, (c) r/d = 1.5 ・・・66

Fig. 3.18 First POD mode of axial velocity fluctuations near elbow outlet (x/d = 0.5) (a) r/d = 1.0, (b) r/d = 1.2, (c) r/d = 1.5 ・・・67

Fig. 3.A-1 Illustration of image deformation ・・・70

Fig. 3.A-2 Radial distribution of magnification factor ・・・70

Fig. 3.B-1 Cross-sectional mean velocity upstream of elbow ・・・71

(a)Mean velocity contour, (b) Radial distribution
Fig. 3.B-2 Cross-sectional turbulence energy distribution upstream of elbow ・・・71
(a)Axial turbulence intensity contour, (b) Radial distribution
Fig. 4.1 Illustration of 90° short elbow ・・・76
(a) Side view, (b) Cross sectional view
Fig. 4.2 Experimental apparatus for mass transfer measurement ・・・77
Fig. 4.3 Experimental test section for velocity measurement ・・・79
Fig. 4.4 Cross-sectional mass transfer distributions in short elbow ・・・84
(a)Re =3×10^4, (b)Re =5×10^4, (c)Re =1×10^5,
(d) Comparison with long elbow (α=90°)
Fig. 4.5 Mean velocity contours in and downstream of short elbow ・・・88
(a)Re =3×10^4, (b)Re =5×10^4, (c)Re =1×10^5
Fig. 4.6 Mean velocity distribution in and downstream of short elbow ・・・88
Fig. 4.7 Axial turbulence intensity contour in and downstream of short elbow
(a)Re =3×10^4, (b)Re =5×10^4, (c)Re =1×10^5 ・・・89
Fig. 4.8 Axial turbulence intensity distributions in and downstream
of short elbow ・・・89
Fig. 4.9 Example of mean velocity profile near separation point ・・・90
Fig. 4.10 Downstream variation of separating flow region in and
downstream of short elbow ・・・90
Fig. 4.11 Near-wall mean velocity contour in horizontal cross section ・・・91
(a)Re =3×10^4, (b)Re =5×10^4, (c)Re =1×10^5
Fig. 4.12 Near-wall axial turbulence intensity contour in horizontal
cross section
(a)Re =3×10^4, (b)Re =5×10^4, (c)Re =1×10^5 ・・・91

List of tables

Table 1.1 Summary of the experimental conditions ・・・14
Table 1.2 Experiments of flow field in a 90° elbow ・・・15
Table 3.1 Fluctuating energy level of POD modes ・・・67

Nomenclature

c	concentration [kg/m^3]
c_b	concentration in bulk flow [kg/m^3]
c_w	concentration on wall [kg/m^3]
d	pipe diameter [m]
K	mass transfer coefficient [m/s]
K_0	mass transfer coefficient in straight pipe [m/s]
K/K_0	amplitude of mass transfer coefficient [-]
k	turbulence energy [m^2/s^2]
r	pipe radius of curvature [m]
r/d	index of radius to pipe diameter ratio [-]
Re	Reynolds number (= Ud/ν) [-]
U	bulk velocity [m/s]
u, v, w	mean velocity components in x,y,z direction, respectively [m/s]
u'	root mean square of axial turbulence intensity
u_i	instantaneous velocity in axial direction [m/s]
v'	root mean square of wall-normal turbulence intensity
$-\overline{u'v'}$	Reynolds stress
x, y, z	coordinate axis in elbow geometry [m]
x_u	coordinate axis from elbow inlet [m]
M	local magnification rate from refractive distortion in the elbow [-]
y'	y coordinate axis from elbow wall [m]
y_+	wall cordinate of roughness height [-]
x/d	index of distance from the elbow outlet [-]
α	progressing angle of elbow arc length [°]
$\delta h/\delta t$	wall thinning rate [m/s]
θ	circumferential angle [°]
ν	kinematic viscosity of fluid [m^2/s]
ρ	density of water [kg/m^3]
ρ_b	density of plaster [kg/m^3]
Φ	1st POD mode of axial velocity fluctuations

Chapter 1

Introduction

1.1 Background

The pipe-wall thinning in the pipeline elements, such as elbow, orifice and tee junction, in the nuclear/fossil power plants is an important topic of interests in the safety management of the power plants. The main cause of the wall thinning is due to the flow accelerated corrosion (FAC), which is a corrosion phenomenon caused by the diffusion of iron ions from the wall into the turbulent bulk flow through the oxide layer over the pipe wall (Keller, 1974, Sydberger and Lots, 1982, Sanchez-Caldera, 1984, Dooley, 2008, Hwang et al., 2009). Although FAC is affected by the water chemistry, the wall-thinning rate is highly correlated with the mass transfer phenomenon driven by the concentration difference of the iron ions in the pipe wall and the bulk flow (Sydberger and Lots, 1982).

In 2004 the pipe break accident occurred in Mihama nuclear power station, which is known to be caused by the FAC. The pipeline layout is illustrated in Fig. 1.1. The pipe diameter of the Mihama nuclear power plant is 600mm with 10mm wall thickness, which is made of a carbon steel material. The working fluid is a high temperature water at 180 degrees C. Therefore, the Reynolds number of working fluid is 5.8×10^6. The pipe break was occurred at 1d downstream of orifice of the A line, which is shown by the picture in Fig. 1.2. It should be mentioned that the A-line consists of a tee and two elbows upstream of the orifice. The cross-section of the break position shows a non-axisymmetric pipe-wall thinning and a pipe break occurs near the top of the pipe, as illustrated in Fig. 1.1. On the other hand, a uniform

pipe-wall thinning was observed in the B-line, in spite of the presence of orifice, elbow and tee. According to the scale-down experiment (NISA 2005), the swirling flow was reported in the A-line, while there was no swirl in the B-line.

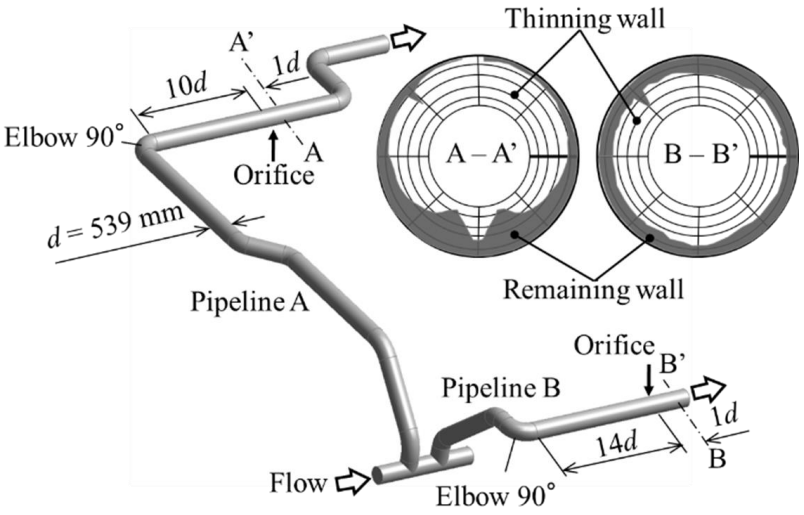

Fig. 1.1 Pipe-line layout of Mihama nuclear power plant

Fig. 1.2 Picture of pipe break at Mihama nuclear power plant

Since the pipe break accident of Mihama nuclear power station, the experimental and numerical studies are carried out to elucidate the mechanism of FAC by evaluating the mass transfer characteristics of the pipeline elements, such as elbow and tee (Yoneda et al. 2008, Ahmad 2010, El-Gammal et al. 2010, Kojo et al. 2011, Uchida et al. 2011, Pietralik 2012, Utanohara et al. 2012, Ahmed et al. 2012, Shan et al. 2013, Yamagata et al. 2014, Shan et al. 2014). It is known that the peak mass transfer coefficient in a pipe downstream of an orifice is three times higher than that of the straight pipe and the position is 1-2 diameters downstream of the orifice in agreement with the observation in the case of Mihama power plant, where the pipe break occurred (NISA 2005). On the other hand, the peak mass transfer coefficient is known to be enhanced by the presence of the swirling flow in the pipeline, so that the combined influence of swirling flow on the complex pipeline geometry with elbow and orifice, has been studied both experimentally and numerically (Fujisawa et al. 2012a, 2012b, Takano et al. 2013, Fujisawa et al 2015a, 2015b, Takano et al. 2016, Fujisawa et al. 2017). These results indicate that the peak mass transfer coefficient of such pipeline elements grows more than several times larger than that in the straight pipe and the mass transfer coefficient becomes non-axisymmetric in circumferential direction. Therefore, the swirling flow plays an important role in the wall-thinning phenomenon of the pipeline. It should be mentioned that the main features of mass transfer coefficient downstream of an orifice is well reproduced by the numerical simulation with the aid of standard k-ε model of turbulence, while there exists some discrepancies in the prediction of peak mass transfer coefficient in the high Schmidt number flows (Yamagata et al. 2014).

Although there are a large number of experiments on the mass transfer characteristics downstream of an orifice (Sydberger and Lots 1982, Yoneda et al. 2008, Ahmad 2010, El-Gammal et al. 2010, Kojo et al. 2011, Utanohara et al. 2012, Ahmed et al. 2012, Shan et al.

2013, Yamagata et al. 2014, Shan et al. 2014, Fujisawa et al. 2012a, 2012b, Takano et al. 2013, Fujisawa et al 2015a, 2015b, Takano et al. 2016, Fujisawa et al. 2017), much less experimental studies are conducted in and downstream of an elbow (Achenbach 1976, Sparrow and Chrisler 1986, Poulson and Robinson 1988, Mazhar et al. 2013). This is mainly due to the difficulty in measuring the mass transfer characteristics inside the elbow experimentally. The mass transfer characteristics of the elbow are known to be highly dependent on the elbow geometry, such as the radius to pipe diameter ratio and the progressing angle from elbow arc length. Furthermore, it is highly affected by the Reynolds number and Schmidt number, so that it is very difficult to understand the mass transfer mechanism by the limited number of experimental data in literature (Achenbach 1976, Sparrow and Chrisler 1986, Poulson and Robinson 1988, Mazhar et al. 2013). Therefore, the detailed measurements of the mass transfer coefficient distribution in the elbow are important to understand the mass transfer mechanism. The mass transfer measurements of elbow are summarized in Table 1.1.

Achenbach (1976) first reported the axial distribution of wall mass transfer coefficient on a 90° elbow of radius to diameter ratio 1.5 (long elbow) at Reynolds number $Re=4\times10^4$ and 3.9×10^5 and Schmidt number Sc=2.53, where the naphthalene sublimation method was used in a working fluid air. The mass transfer measurements were carried out along the axial direction and the result indicates that the mass transfer enhancement is observed on the first half of the inner wall and the second half of the outer wall, which was found to be closely related to the wall shear stress distributions along the wall. However, the change of the mass transfer distribution was noticed by the experiments at two different Reynolds numbers, which suggested the presence of different flow pattern in the elbow depending on the Reynolds number. More recently, Mazhar et al. (2013) investigated the mass transfer characteristics on a 90° elbow with a radius to diameter ratio 1.5 and at Schmidt number 1280 in the range of

Reynolds number 4×10^4-1.3×10^5 using the plaster dissolution method in a working fluid of water. The diameter of the test pipe is 25.4mm, while the removed plaster layer is rather thick (1 to 2mm) in the mass transfer measurements. They reported not only the axial distribution but also azimuthal distribution of Sherwood number, and they showed a mass transfer enhancement at the first half of the inner wall and the second half of the outer wall. However, the experimental data were highly scattered from the average value ±18% due to the unexpected uncertainty of mass transfer measurement, which may be due to the three-dimensional measurement of wall thinning distribution on the target elbow. Furthermore, their experimental result suffered from the surface roughness effect as was mentioned in the paper, so that the flow through the elbow could be in a hydraulic rough wall region. These past studies on the mass transfer measurements on the long elbow showed that the flow through the elbow was highly complex and it was rather difficult to understand the mass transfer characteristics in the 90° elbow. It should be mentioned that the characteristics of pressure loss in the 90° elbow was summarized in review papers (Spedding et al. 2004, Crawford et al. 2007) and the turbulence measurements in the elbow were reported in the literature (Enayet et al. 1982, Anwar and So 1993, Sudo et al. 1998, Iwamoto et al. 2010, Yuki et al. 2011, Ono et al. 2011), which were fundamentals of the mass transfer studies in the elbow.

Table 1.1 Summary of the experimental conditions

	Radius to diameter ratio (r/d)	Reynolds number	Schmidt number	Experimental method (working fluid)	Surface condition
Achenbach (1976)	1.5	$Re = 9\times10^4$, 39×10^4	Sc=2.53 (Air)	Naphthalene sublimation (air)	Smooth
Mazhar et al. (2013)	1.5	$Re = (4\text{-}13)\times10^4$	Sc=1280 (Water)	Plaster dissolution (water)	Rough
Chapter 2	1.5	$Re = 5\times10^4$	Sc=680 (Water)	Plaster dissolution (water)	Smooth
Chapter 4	1.0	$Re = (3\text{-}10)\times10^4$	Sc=680 (Water)	Plaster dissolution (water)	Smooth

In the past, mean flow and turbulence measurements in a 90° elbow were carried out at moderate Reynolds numbers, Re = (4 to 32) × 10^4 (Enayet, 1982; Sudo et al., 1998; Iwamoto et al., 2010; Yuki et al., 2011; Mazhar et al., 2016; Taguchi et al., 2018). These measurements are summarized in Table 1.2. On the other hand, there are fewer studies on elbow flow in the post-critical Reynolds numbers beyond Re=4× 10^5, where flow characteristics are expected to be independent of the Reynolds number (Ono et al., 2011; Iwamoto et al., 2012; Ebara et al., 2016). It should be mentioned that the difficulty of velocity field measurement in the elbow is caused by the presence of curved surface of the elbow, which causes the refractive index difference at the interface of elbow material and the working fluid.

Furthermore, numerical studies on elbow flows at high Reynolds numbers were

carried out to understand the flow phenomena (Tanaka and Ohshima, 2012; Dutta et al., 2016). These past studies were conducted on elbows of different elbow radius to diameter ratios ranging from r/d = 1.0 to 2.8 and Reynolds numbers ranging from Re = (4.3 to 32) × 10^4.

Among these past studies, the results of experiments on the flow in elbows with radius ratios between 1.0 (short elbow) and 1.5 (long elbow) are frequently used in power plant pipelines. However, the mass transfer characteristics of the 90° short elbow has not been reported in the literature, in spite of its importance in application to power plant. Thus, the effect of elbow curvature and the Reynolds number on mass and momentum transfer characteristics of the 90° elbow is not so well understood in literature, while these knowledges are very important to understand the mass and momentum transfer in 90° elbow.

Table 1.2 Experiments of flow field in a 90° elbow

Authors (Year)	Radius to diameter Ratio (r/d)	Reynolds Number Re	Measurement Technique
Enayet et al. (1982)	2.8	4.3 × 104	LDV
Sudo et al. (1998)	2.0	6 × 104	Hot wire
Iwamoto et al. (2010, 2012)	1.0	5 × 104,3.2 × 105	LDV
Yuki et al. (2011)	1.0	5 × 104	Matched refractive index Planar PIV
Mazhar et al. (2016)	1.5	4 × 104, 7 × 104	Matched refractive index Planar PIV
Taguchi et al. (2018)	1.5	(5-20) × 10^4	Planar PIV
Chapter 3	1.0, 1.2, 1.5	(3-10) × 10^4	Planar PIV, Stereo PIV
Chapter 4	1.0	(3-10) × 10^4	Planer PIV

1.2 Purpose of this research

In the present thesis, the mass and momentum transfer characteristics are experimentally studied in and downstream of the a 90° elbow, where the radius to diameter ratio is r/d=1.0, 1.2, and 1.5 and Reynolds number ranges Re = (3-15)×10^4. The results are compared with the surface flow visualization by the oil film method and the PIV velocity measurement to elucidate the curvature effect and Reynolds number effect on mass and momentum transfer characteristics in and downstream of the elbow.

In chapter 2, the mass transfer characteristics of a 90° long elbow (radius to diameter

ratio : r/d= 1.5) was studied experimentally using the plaster dissolution method. Furthermore, the surface flow visualization and the velocity measurement by PIV were carried out to understand the mechanism of mass transfer in and downstream of a 90° elbow.

In chapter 3, the velocity field through a 90° elbow was measured by a PIV for various combinations of radius to diameter ratios and Reynolds numbers and the variations of the mean and turbulence characteristics with the elbow curvature and the Reynolds number were examined experimentally. Furthermore, turbulence structure downstream of the pipe was examined by proper orthogonal decomposition (POD) analysis combined with the stereo PIV measurement, which tells the variation of turbulence structure with the radius to diameter ratio and Reynolds number.

In chapter 4, the mass transfer distribution in a 90° short elbow (r/d= 1.0) were investigated experimentally in the Reynolds number range Re = $(3\text{-}15)\times10^4$. Furthermore, the flow field near the inner wall was studied by particle image velocimetry (PIV) measurements, which allows the variation of the separation and reattachment points on the inner wall of the elbow with the Reynolds number. An attention is placed on the mass transfer characteristics and the flow separation behavior on the inner wall of the short elbow.

Chapter 5 is the conclusion of this thesis, and the mass and momentum transfer characteristics in the elbow is described in relation to pipe-wall thinning phenomenon.

References

Abe, H., Watanabe Y., Nakashima, M, Tatsuki, T., 2017. Characterization of the corroded surface morphology of a carbon steel piping elbow affected by flow-accelerated corrosion. E-J. Adv. Mainte., 9, 26-32.

Ahmed, W.H., Bello, M. M., Nakla, M.E., Sarkhi, A.A., 2012. Flow and mass transfer downstream of an orifice under flow acclerated corrosion conditions. Nucl. Eng. Des. 252, 52-67.

Anwar, M., So, R.M.C., Swirling turbulent flow through a curved pipe, Exp. Fluids, 14(1993), 85-96.

Berkooz, G., Holmes, P., Lumley, J.L., 1993. The proper orthogonal decomposition in the analysis of turbulent flows. Annu. Rev. Fluid Mech. 25, 539–575.

Bernero, S., Fielder, H.E., 2000. Application of particle image velocimetry and proper orthogonal decomposition on the study of a jet in counterflow. Exp. Fluids. 29, S274–S281.

Dooley, R.B., Chexal, V.K., 2000. Flow-accelerated corrosion of pressure vessels in fossil plants. Int. J. Pressure Vessels and Piping. 77, 85-90.

Dutta, P. Saha, S. K. Nandi, N., Pal, N. 2016. Numerical study on flow separation in 90° pipe bend under high Reynolds number by k-ε modelling. Eng. Sci. Tech., Int. J. 19, 904-910.

Ebara, S., Takamura, H., Hashizume, H., Yamano, H., 2016. Characteristics of flow field and pressure fluctuation in complex turbulent flow in the third elbow of a triple elbow piping with small curvature radius in three-dimensional layout. Int. J. Hydrogen Energy, 41, 7139-7145.

Enayet, M.M., Gibson, M.M., Taylor, A.M.K.P., Yianneskis, M., 1982. Laser-doppler

measurements of laminar and turbulent flow in a pipe bend. Int. J. Heat Fluid Flow. 3, 213-219.

El-Gammal, M., Mazhar, H., Cotton, J.S., Shefski, C., Pietralik, J., Ching, C.Y., 2010. The hydrodynamic effects of single-phase flow on flow accelerated corrosion in a 90° elbow, Nucl. Eng. Des. 240, 1589–1598.

Fujisawa, N., Yamagata, T., Kanno, S., Ito, A., Takano, T., 2012. The mechanism of asymmetric pipe-wall thinning behind an orifice by combined effect of swirling flow and orifice bias. Nucl. Eng. Des. 252, 19-26.

Fujisawa, N., Kanatani, N., Yamagata, T., Takano, T., 2015. Mechanism of non-axisymmetric pipe-wall thinning in pipeline with elbow and orifice under influence of swirling flow, Nucl. Eng. Des. 285, 126-133.

Fujisawa, N., Yamagata, T., Kanatani, N., Watanabe, R., 2015. Non-axisymmetric wall-thinning downstream of elbow-orifice pipeline in swirling flow, Ann. Nucl. Energy, 80, 356-364.

Fujisawa, N., Uchiyama, K., Yamagata, T., 2017. Mass transfer measurements on periodic roughness in a circular pipe and downstream of orifice, Int. J. Heat Mass Transfer, 105, 316-325.

Funatani, S., Fujisawa,N., 2002. Simultaneous measurement of temperature and three velocity components in planar cross-section by liquid crystal thermometry combined with stereoscopic particle image velocimetry. Meas. Sci. Technol. 13, 1197-1205.

Hwang, K.M., Jin, T.E., Kim, K.H., 2009. Identification of the relationship between local velocity components and local wall thinning inside carbon steel piping. J. Nuc. Sci. Technol. 46, 469-478.

Ikarashi, Y., Taguchi, S., Yamagata, T., Fujisawa, N., 2017. Mass and momentum transfer characteristics in and downstream of 90° elbow, Int. J. Heat Mass Transfer. 107, 1085-1093.

Iwamoto, Y., Minamiura, H., Sogo, M., Yamano, H., 2010. LDV measurements of a flow in a strongly-curved elbow under a high Reynolds number condition. Trans. Japan Soc. Mech. Eng. 76, 830-838. (in Japanese)

Iwamoto, Y., Kondo, M., Minamiura, H., Tanaka, M., Yamano, H., 2012. Unsteady flow characteristics in a 90 degree elbow affected by developed, undeveloped and swirling inflow conditions, J. Fluid Sci. Technol. 7, 315-328.

Keller, V.H., 1974. Erosionskorrosion Nabdampfturbien. VGB-Kraftwerkstechnik. 54, 292-295.

Kiuchi, M., Fujisawa, N. Tomimatsu, S., 2005. Performance of a PIV system for a combusting flow and its application to spray combustor model. J. Vis. 8, 269-276.

Kostas, J., Soria, J., Chong, M.S., 2005. A comparison between snapshot POD analysis of PIV velocity and vorticity data. Exp. Fluids. 38, 146–160.

Mazhar, H., Ewing, D., Cotton, J.S., Ching, C.Y., 2013. Experimental investigation of mass transfer in 90° pipe bends using a dissolvable wall technique, Int. J. Heat Mass Transfer. 65, 280–288.

Mazhar, H., Ewing, D., Cotton, J.S., Ching, C.Y., 2016. Measurement of the flow field characteristics in single and dual S-shape 90° bends using matched refractive index PIV, Exp. Therm. Fluid Sci. 79, 65-73.

Nguyen, T., Goth N., Jones, P., Vaghetto, R., Hassan, Y., 2018. Stereoscopic PIV measurements of near-wall flow in a tightly packed rod bundle with wire spacers, Exp. Therm. Fluid Sci., 92, 420-435.

NISA, 2005. Secondary piping rupture accident at Mihama power station, unit 3, of the Kansai electric power co. inc. (Final Report).

Ono, A., Kimura, N., Kamide, H., Tobita, A., 2011. Influence of elbow curvature on flow structure at elbow outlet under high Reynolds number condition. Nucl. Eng. Des. 241, 4409-4419.

Pietralik, J.M., 2012. The role of flow in flow-accelerated corrosion under nuclear power plant conditions. E-J. Adv. Mainten. 4, 63-78.

Shan, F., Fujishiro, A., Tsuneyoshi, T., Tsuji, Y., 2014. Effects of flow field on the wall mass transfer rate behind a circular orifice in a round pipe, Int. J. Heat Mass Transer. 73, 542-550.

Sanchez-Caldera, L.E., 1984. The mechanism of corrosion-erosion in steam extraction lines of power station. Ph.D. Thesis, Dept. Mech. Eng., M I T, Cambridge, Massachusetts.

Sudo, K., Sumida, M., Hibara, H., 1998. Experimental investigation on turbulent flow in a circular-sectioned-90-degree bend. Exp. Fluids. 25, 42-49.

Sydberger, T., Lotz, U., 1982. Relation between mass transfer and corrosion in a turbulent pipe flow. J. Electrochem. Soc. 129, 276-283.

Taguchi, S., Ikarashi, Y., Yamagata, T., Fujisawa, N., Inada, F., 2018. Mass and momentum transfer characteristics in 90° elbow under high Reynolds number, Int. Comm. Heat Mass Transfer. 90, 103-110.

Takano, T., Yamagata, T., Sato, Y., Fujisawa, N., Non-axisymmetric mass transfer phenomenon behind an orifice in a curved swirling flow, J. Flow Control Meas. Vis. 1(2013), 1-5.

Tanaka, M., Ohshima, H., 2012. Numerical investigation on large scale eddy structure in unsteady pipe elbow flow at high Reynolds number conditions with large eddy simulation approach. J. Power Energy Syst. 6, 210-228.

Utanohara, Y., Nagaya, Y., Nakamura, A., Murase, M., 2012. Influence of local flow field on flow accelerated corrosion downstream from an orifice. J. Power Energy Syst. 6, 18-33.

Wang, D., Ewing, D., Ching, C.Y., 2016. Time evolution of surface roughness in pipes due to mass transfer under different Reynolds numbers. Int. J. Heat Mass Transf., 103, 661-671.

Wieneke, B., 2015. PIV uncertainty quantification from correlation statistics. Meas. Sci. Technol. 26, 074002.

Yamagata,T., Ito, A., Sato,Y., Fujisawa, N., 2014. Experimental and numerical studies on mass transfer characteristics behind an orifice in a circular pipe for application to pipe-wall thinning. Exp. Therm. Fluid Sci. 52, 239-247.

Yoneda, K., Morita, R., Satake, M., Inada, I., Quantitative evaluation of effective factors on flow accelerated corrosion (part 2), Modelling of mass transfer coefficient with hydraulic features at wall, CRIEPI Res. Rep., No. L07015(2008), 1-33.(in Japanse)

Yuki, K., Hasegawa, S., Sato, T., Hashizume, H., Aizawa, K., Yamano, H., 2011. Matched refractive index visualization of complex flow structure in a three dimensionally connected dual elbow. Nucl. Eng. Des. 241, 4544-4550.

Chapter 2

Mass and Momentum Transfer Characteristics of 90° Long Elbow

2-1 Introduction

In this chapter, the mass and momentum transfer characteristics of a 90° elbow with mild curvature were experimentally studied by using the plaster dissolution method. Furthermore, the velocity measurement by PIV and the surface flow visualization were carried out to understand the mechanism of mass transfer in and downstream of a 90° elbow.

2.2. Experimental apparatus and procedures

2.2.1 Experimental set-up

The experimental studies on mass and momentum transfer characteristics in and downstream of an elbow have been carried out in a closed-circuit water tunnel. A schematic layout of the water tunnel is shown in Fig. 2.1, which consists of a tank with temperature controller, pump, settling chamber, straight pipe and a test elbow. The diameter of the test pipe is set to d = 56 mm and the radius to diameter ratio of the elbow is 1.5, which is a long elbow for application to power plant. The straight pipe upstream of the elbow was set to 24d for the flow development.

The experiments were carried out with a working fluid water at temperature 303K and the bulk flow velocity is set to U=0.72m/s, so that the Reynolds number Re (= Ud/v) was kept constant Re= 5×10^4, while the Schmidt number of this experiment was

680 in the mass transfer measurements. The experimental Reynolds number of this study was determined in reference to the past experiments on turbulence measurements in elbow (Enayet et al. 1982, Anwar and So 1993, Sudo et al. 1998, Iwamoto et al. 2010, Yuki et al. 2011), while Mazhar et al. (2013) showed the Reynolds number independence on the mass transfer characteristics in the range Re= (4-13)× 10^4.

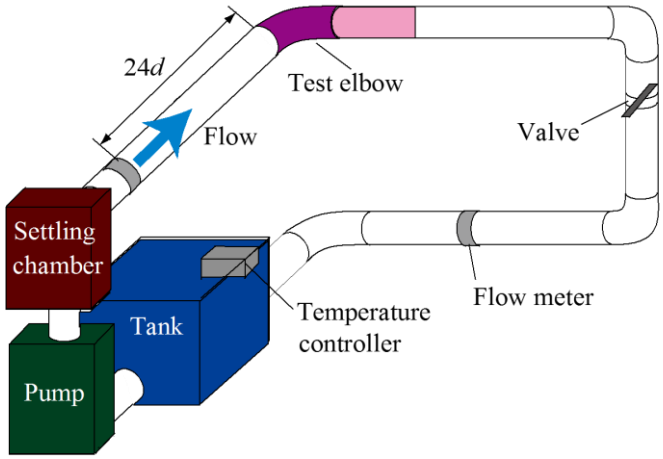

Fig. 2.1 Schematic layout of water tunnel and test elbow

2.2.2 Test elbow for mass transfer measurement

Figure 2.2(a) shows an illustration of the test elbow geometry for mass transfer measurement in the present study. The mass transfer measurements are carried out at 5 cross sections of the elbow perpendicular to the wall at α=0, 22.5, 45, 67.5, 90°, where α is defined by the angle measured from the inlet of the elbow. In order to measure the mass transfer distribution on the cross section of the elbow with high accuracy, two kinds of test elbow are constructed, one is for measurement on inner and outer walls of elbow and the others are for measurement on the side walls of the elbow, which are illustrated in Fig. 2.2(b). This is mainly due to the necessity of high accuracy

measurement of wall thinning distribution. This can be achieved in a limited angle ranging from -45－45° in the central region of the test section corresponding to 1/4 of the whole circular angle θ. These elbows are made of two half pipes separated at the vertical center plane and the horizontal center plane to measure the cross sectional mass transfer distributions. These test elbows are made of resin material produced by a 3D printer, and the wall surfaces are polished by emery papers #1000 to smooth the wall. The depth of the plaster layer on the wall was maintained to 2mm thick and the casting was supported by the mold of the resin made by the 3D printer. The surface of the plaster layer on the elbow was also polished by the emery paper to be smooth enough to accomplish the mass transfer measurement. The measurements are carried out on each half pipe elbows and the mass transfer distribution in the whole circumferential angles is reconstructed from the measurements on the 4 half pipes. It should be mentioned that the gas bubbles generated in the plaster layer produces the roughness on the plaster layer, so that they are removed from the plaster layer using the vacuum pump in the preparation of the liquid plaster. The pictures of the test elbow used in this experiment are shown in Figs. 2.3(a)-(c), which correspond to the inner, outer and side walls, respectively.

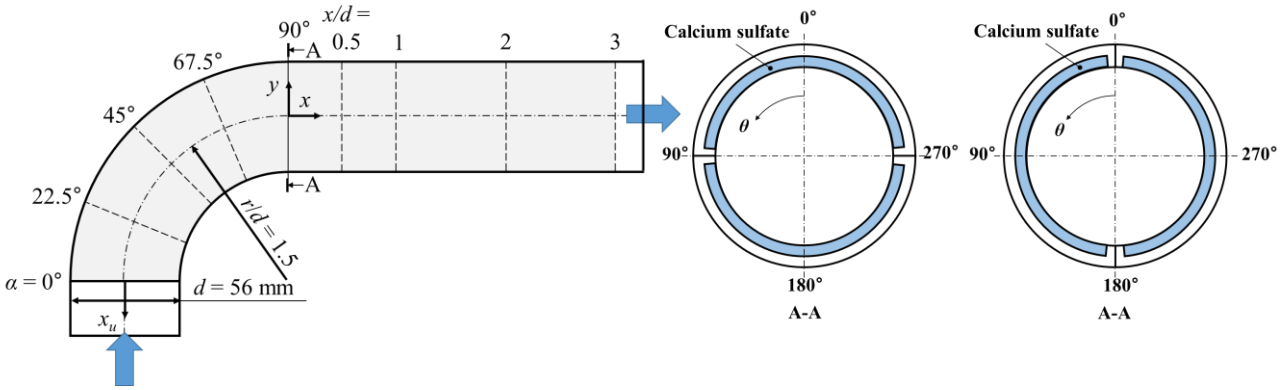

(a) Test elbow geometry (b) Inner - outer and side walls

Fig. 2.2 Design of test elbow for mass transfer measurement

(a) Inner wall (b) Outer wall (c) Side wall

Fig. 2.3 Pictures of test elbows for mass transfer measurement

2.2.3 Measurement of mass transfer characteristics

The experimental arrangement for measuring the wall thinning distribution on the plaster layer is shown in Fig. 2.4, which consists of the traversing device driven by stepping motor, laser displacement sensor and the test section of the half elbow. In order to set the half elbow on the base structure of the traversing devise with high accuracy,

the half elbow is fixed to the base structure through the taper pins, which allow the accurate setting of the half elbow on the base structure within an accuracy of 10μm. The depth distribution of the plaster layer is detected by the laser displacement sensor (spatial resolution 1μm). The half elbow on the base structure was traversed driven by a stepping motor, while the position of the laser displacement sensor was fixed in space. The wall thinning measurement was carried out at 5 cross sections in the elbow (α=0, 22.5, 45, 67.5, 90°) and 4 cross sections downstream of the elbow in a straight pipe (x/d=0.5, 1, 2, 3), while the 4 axial traverses were done for mass transfer measurements along the inner and outer wall and side walls for every 90° in circumferential direction in the straight pipe section.

The mass transfer coefficient was evaluated from the wall thinning distribution of the plaster layer on the elbow, which was obtained from the surface contour measurement normal to the wall before and after the experiment. It should be mentioned that the wall thinning distribution normal to the elbow wall was evaluated from the measured depth distribution by correcting the influence of inclination angle of the wall. The mass transfer coefficient K was obtained from the following equation;

$$K = \frac{\rho_b \delta h / \delta t}{c_w - c_b} \tag{1}$$

where $\delta h/\delta t$ is the wall-thinning rate of the plaster layer in a unit time, ρ_b is the density of plaster layer, c_w is the concentration of the plaster layer, c_b is the concentration of the dissolved plaster in bulk flow. Note that c_w is assumed as the saturated concentration of the dissolved plaster and c_b is evaluated from the volume of dissolved plaster in the bulk flow. Note that the dissolved concentration of the plaster in the bulk flow is measured by the concentration meter and is kept less than 10% of the saturated concentration of

the plaster in water. The uncertainty in the measurement of the mass transfer coefficient was estimated as 5.6% in the confidence level of 95%. The major error comes from the position error 10μm of the test section for wall thinning measurement, while there is a minor error in the concentration measurement 2%, the time derivative error 1% and the bias error in depth measurement by laser displacement sensor 0.25%. The surface roughness on the plaster layer after the experiment is found to be 4 μm in RMS roughness, which corresponds to the wall coordinate of roughness height y_+=0.2, so that the flow on the elbow is considered hydraulically smooth. Note that a typical example of the maximum wall thinning of the plaster layer is 300μm in an elapsed time of 1 hour.

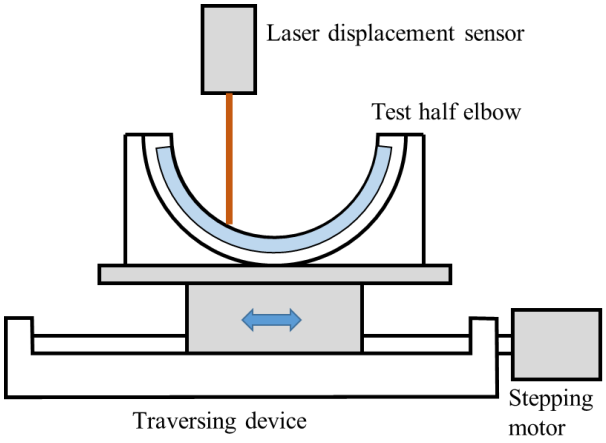

Fig. 2.4 Experimental test section for mass transfer measurement

2.2.4 Surface flow visualization by oil film method

In order to understand the flow field in the elbow, the surface flow visualization by oil film method was carried out inside the elbow. The composition of the oil used in this experiment is the liquid paraffin, oxide titanium and the oleic acid, which are mixed in the weight ratio 3:1:2, respectively, while the pipe wall is colored black to enhance

the contrast. The oil points are distributed on the elbow wall with a weight of 2.5 μl per point and they are placed on the elbow surface using a micro injector. The surface flow visualization on the elbow was carried out at the same Reynolds number as the mass transfer measurement.

2.2.5 Measurement of velocity field by SPIV

The cross sectional velocity field downstream of the elbow was measured by the stereo particle image velocimetry, which consists of two CCD cameras, Nd:YAG pulse laser, pulse controller and calibration equipment illustrated in Fig. 2.5. In order to visualize the velocity field, the test section is made transparent using an acrylic resin material and the nylon tracer particles are added to the working fluid water. The diameter of the nylon tracer is 40 μm and the specific gravity is 1.02. The SPIV system allows the measurement of three velocity components in the cross-section of interest at four axial positions x/d = 0.5, 1, 2, and 3 downstream of the elbow. The flow observation was made by two CCD cameras through the water jackets on both sides of the pipe to minimize the influence of refractive index difference at the interface of the working fluid water and the acrylic resin material of circular pipe wall. These CCD cameras are situated in Scheimpflug configuration with inclined angles ±45°. The SPIV system consists of two CCD cameras with the frame straddling function (1018 × 1008 pixels with 8 bits in gray level), Nd:YAG pulse laser (maximum output power 50 mJ/pulse) and a pulse controller. The light sheet illumination for flow visualization was provided from the top of the test section normal to the pipe axis. The thickness of the light sheet was 2 mm.

The three-dimensional calibration of the stereo cameras were carried out by

traversing the calibration plate, which shows the grid pattern of every 2.5mm interval. Five calibration images are taken for every 0.5mm by traversing the calibration plate in axial direction. The statistical properties of mean and fluctuating velocities were evaluated from 500 instantaneous velocity fields measured at every 0.2 seconds in time interval. The measurements are carried out at the same Reynolds number Re=5 × 10^4 as the mass transfer measurements. The details of the stereo PIV technique and the data analysis has been described in the literature (Raffel et al. 1998, Funatani and Fujisawa 2002, Kiuchi 2005).

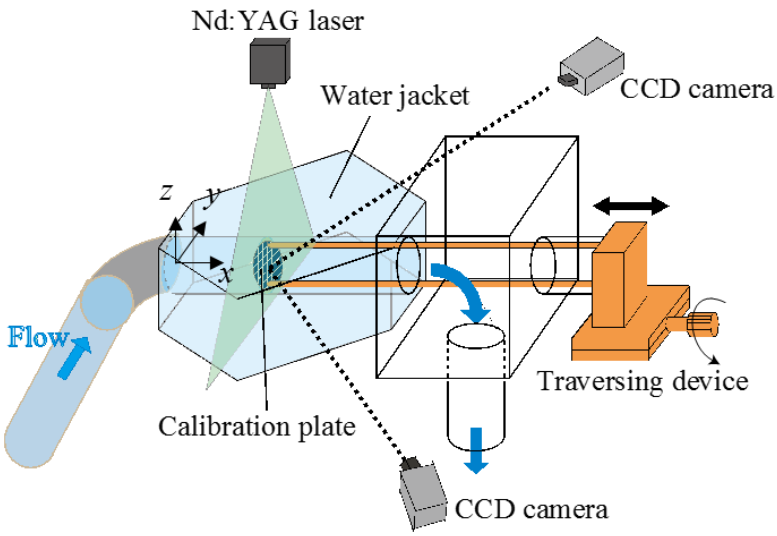

Fig. 2.5 Experimental test section for velocity field measurement

2. 3. Results and discussion

2.3.1 Distributions of mass transfer coefficient on elbow

Figures 2.6(a)-(e) show the cross-sectional distributions of mass transfer coefficient in the test elbow, which are measured by the present plaster dissolution method. The measurements are carried out at Reynolds number Re=5 × 10^4. The

experimental data show the ensemble average of the data over ±5° in circumferential direction of the measured data taken from 4 repeated experiments. Note that the scattering of the data is indicated by the error bars. Each graph shows the magnitude of the local mass transfer coefficient distribution normalized by that of the straight pipe and the angle θ of the circular graph shows the circumferential angle, which is measured from the outer wall of the elbow (Fig. 2.2). Note that the angle θ=0° corresponds to the outer wall position, θ=180° shows the inner wall position and θ=90° and 270 ° are side wall positions.

Figure 2.6(a) shows the mass transfer coefficient distribution at the inlet of the elbow α=0°. The present result indicates that the local mass transfer coefficient on the cross section is only slightly larger than 1. This result indicates that the mass transfer coefficient at the inlet of the elbow agrees closely with that of the straight pipe. On the other hand, the mass transfer distribution (α=22.5°) in Fig. 2.6(b) shows a sharp decrease in the mass transfer coefficient on the inner wall down to 0.6, while it keeps almost constant magnitude slightly larger than 1 on the rest of the wall. With further increase in the cross-sectional angle to α=45° (Fig. 2.6(c)), the mass transfer coefficient in the inner wall remains in a low value 0.7, while the growth of mass transfer coefficient occurs in the neighbor of the inner wall and the rest of the distribution remains the same magnitude as that of α=22.5°. With further increase occurs in the cross-sectional angle to α=67.5°-90° (Fig. 2.6(d)-(e)), the mass transfer coefficient on the inner wall grow to around 1.5 and that on the rest of the circumferential position of the elbow remains the same magnitude as that of the straight pipe. The high mass transfer coefficient in the inner wall spreads around the neighbors in the outlet of the elbow and the rest of the distribution approaches that of the straight pipe (Fig. 2.6(e)).

These results indicate that the major change of the mass transfer coefficient occurs on the inner wall of the elbow.

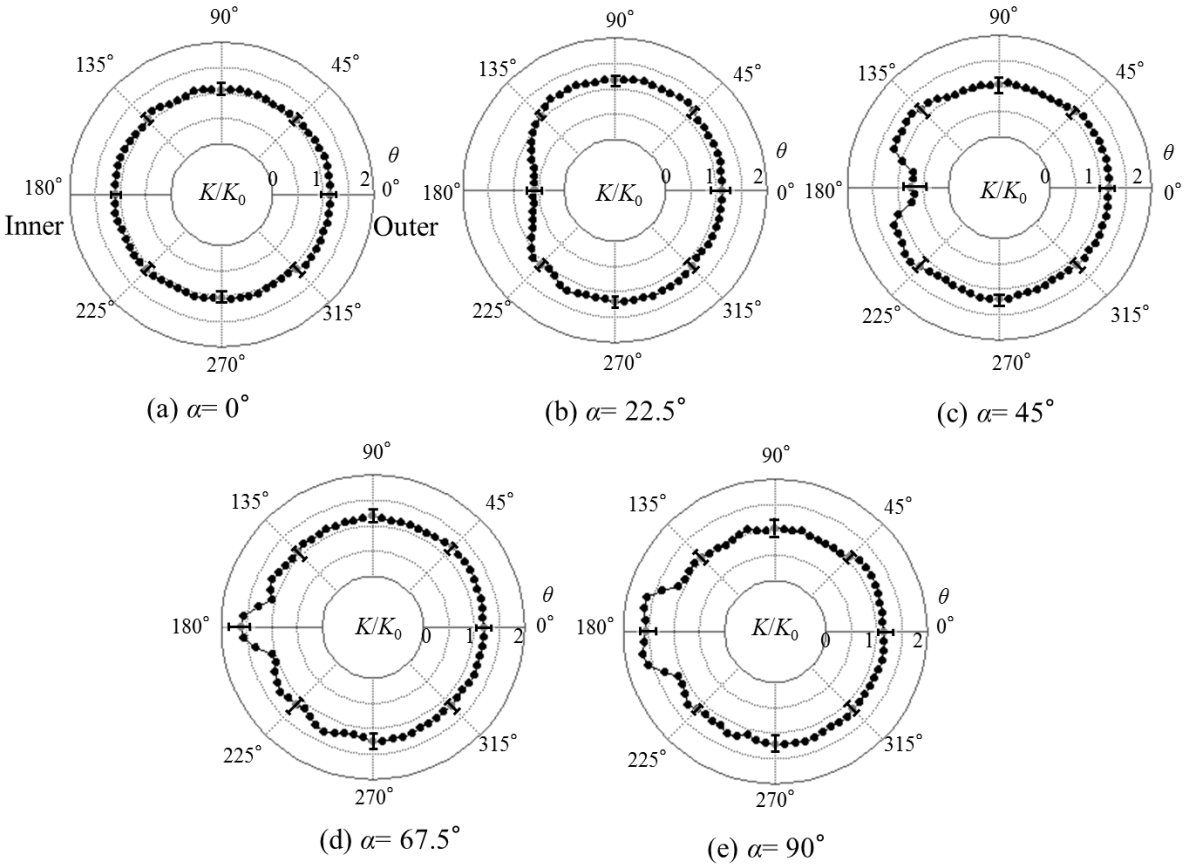

Fig. 2.6 Cross-sectional mass transfer coefficient distributions in elbow

2.3.2 Visualization of surface flow in elbow

The surface flow visualization in the elbow is carried out by using the oil film method and the results are shown in Fig. 2.7 at the same Reynolds number as the mass transfer measurement. These visualization results are on the inner wall (a), outer wall (b) and side wall (c), respectively, which are obtained from the oil displacement on each elbow surface in a time interval of 4 min. Although the surface flow upstream of the elbow directs to the axial direction almost uniformly, the surface flow pattern on the inner wall

(a) shows a convergence of flow pattern from the side to the center of the elbow in the first half of the elbow (α=0-45°), while the flow pattern on the outer wall (b) shows a divergence from the center to the side on the outer wall. Corresponding to the flow pattern on the inner and outer walls, the flow pattern on the side wall shows the surface flow from the outer to the inner wall, which shows the surface trace of the secondary flow generated in the elbow. It should be mentioned that the secondary flow in the elbow is generated by the centrifugal instability of the flow through the elbow, which directs from the inner wall to the outer wall through the pipe center and the return flow is generated on the side wall from the outer to the inner wall, as shown in Fig. 2.7(c). The secondary flow pattern seems to be accelerated on the first half of the elbow and decelerated on the second half on the inner wall of the elbow (c) (α=45-90°), where the flow on the inner wall seems to be separated from the wall, which appears as the small displacement of the oil. However, the surface flow on the inner wall recovers quickly as the flow exits from the elbow downstream. On the other hand, the flow on the outer wall is accelerated in the second half of the elbow. Due to such difference in the flow pattern on the inner and outer walls, the mass transfer coefficient distribution shows the axial variation along the inner and outer wall, as was shown in Fig. 2.6. Thus, the main feature of the mass transfer coefficient distribution in the elbow are well reproduced in the surface flow visualization results. It should be mentioned that the mass transfer enhancement in the second half of the inner wall is due to the combined effect of flow convergence and separation in the inner wall, which may enhance the turbulence energy production near the inner wall. According to the result by Iwamoto et al. (2010) in the elbow of radius to diameter ratio 1 at the same Reynolds number $Re=5\times10^4$, the axial turbulence intensity is found to be high around α=67.5 - 90°, which is measured by the

laser Doppler velocimetry. This result supports the flow separation in the second half of the inner wall.

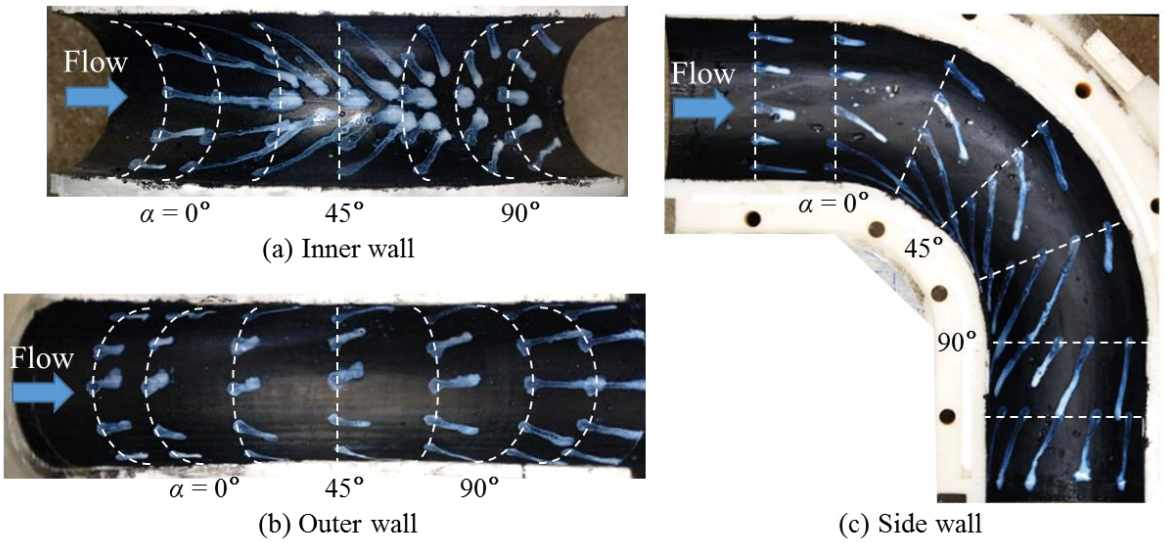

Fig. 2.7 Visualization of surface flow distribution

2.3.3 Distributions of mass transfer coefficient downstream of elbow

Figures 2.8(a)-(c) show the cross-sectional distributions of mass transfer coefficient downstream of the elbow. In the immediate downstream of the elbow at *x/d*=0.5 (Fig. 2.8 (a)), the mass transfer coefficient shows a high peak on the inner wall, while the magnitude remains roughly the same as the straight pipe in the rest of the wall, which is similarly seen in the mass transfer coefficient distribution at the exit of the elbow α=90° in Fig. 2.6 (e). This feature is also observed by the mass transfer coefficient distribution of downstream *x/d*= 1 from elbow (Fig. 2.8 (b)), while the peak magnitude of mass transfer coefficient decreases slightly downstream. With further increase in downstream distance *x/d*=2 and 3, the mass transfer distribution on the inner wall decreases gradually (Figs. 2.8(b),(c)), while the mass transfer coefficient on the other wall tends to

increase slightly in the downstream. These variations of mass transfer coefficients downstream of the elbow shows the recovery of the secondary flow in the elbow.

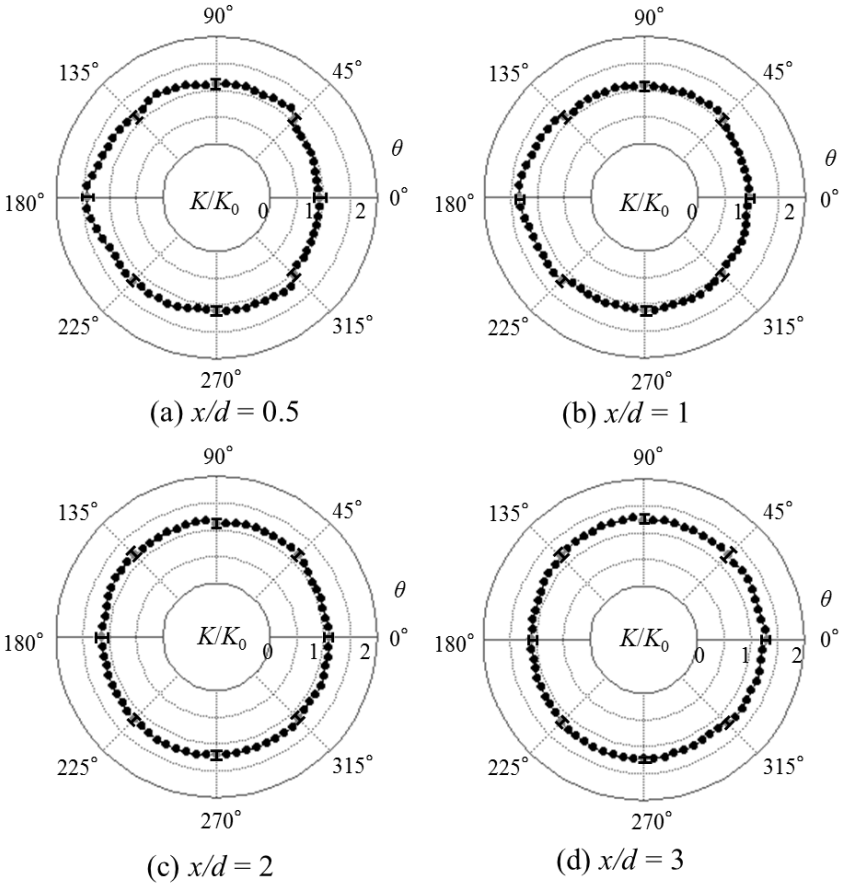

Fig. 2.8 Cross sectional mass transfer distributions downstream of elbow

2.3.4 Mean velocity and turbulence energy downstream of elbow

In order to understand the flow mechanism downstream of the elbow, the cross-sectional distributions of velocity field were measured by the stereo PIV at Re=5 × 10^4. The three-dimensional mean velocity and the turbulence energy at four cross sections *x/d*=0.5, 1, 2, 3 downstream of the elbow are measured and the results are shown in Figs. 2.9 and 2.10, respectively. It should be mentioned that the in-plane mean

velocity field is shown by the vector plots and the out-of-plane mean velocity and the turbulence energy fields are shown by the color contours.

The mean velocity contour near the elbow exit in Fig. 2.9(a) shows the radial flow from the inner to outer wall through the center of the pipe and the return flow back to the inner wall along the side wall of the pipe. Such secondary flow in the elbow is caused by the centrifugal instability of the curved flow in the elbow and the resulted pressure gradient. On the other hand, the high axial velocity is observed near the outer wall of the pipe and the low axial velocity is found near the inner wall of the pipe. Note that the mean velocity contour is symmetric with respect to the central plane of the elbow. With increasing the downstream distance from the elbow to x/d=1 (Fig. 2.9(b)), the high axial velocity region moves to the outer wall and it develops along the wall, which is followed by the growth of low axial velocity region in the center of the cross section at x/d=2 (Fig. 2.9(c)). These flow features are similarly observed in the cross section further downstream x/d= 3 (Fig. 2.9(d)), which indicates that the secondary flow exists in all the cross sections of measurement in the straight pipe downstream of the elbow.

The turbulence energy contours in the downstream of the elbow are shown in Fig. 2.10(a)-(d) at Reynolds number Re=5 × 10^4. An increase in the turbulence energy is observed in the inner wall of the elbow, while the low turbulence energy is found in the outer wall of the elbow (Fig. 2.10(a)). These results are well correlated with the decrease in axial velocity in the inner wall of the elbow and an increase in axial velocity in the outer wall of the elbow (Fig. 2.9). With increasing the downstream distance from the elbow, the high turbulence energy region grows to the outer wall (Fig. 2.10(b)) and the low turbulence energy region in the outer wall moves to the inner wall along the

side wall (Fig. 2.10(c),(d)). The magnitude of the turbulence energy in the inner wall decreases and that in the outer wall increases with increasing the downstream distance. It seems that the turbulence energy in the outer wall becomes the maximum at x/d=2 and it decreases gradually downstream. This result coincides with that of maximum axial velocity variation in Fig. 2.9. It should be mentioned that the high mass transfer coefficient on the inner wall at the exit of the elbow is highly correlated with the high turbulence energy on the inner wall. This result suggests that the mass transfer enhancement mechanism in the elbow is driven by the turbulence in the secondary flow generated in the elbow.

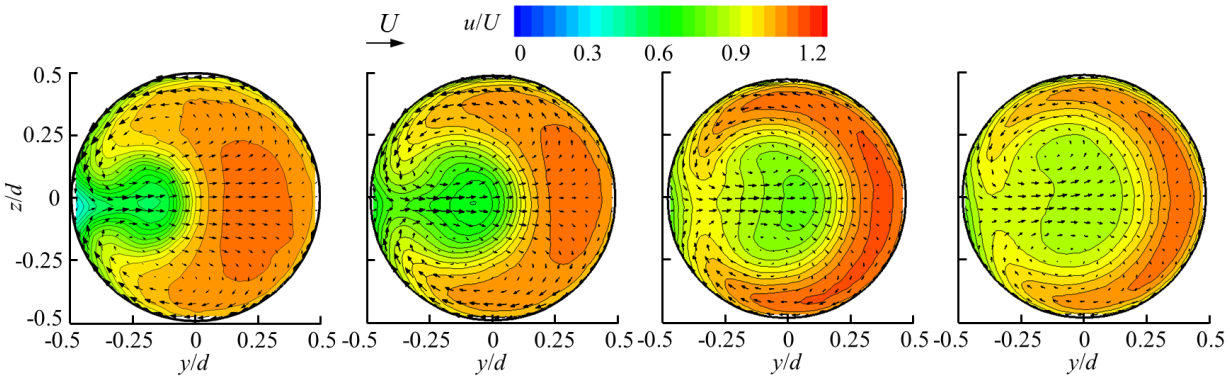

(a) x/d=0.5 (b) x/d=1 (c) x/d=2 (d) x/d=3

Fig. 2.9 Cross-sectional mean velocity contours downstream of elbow

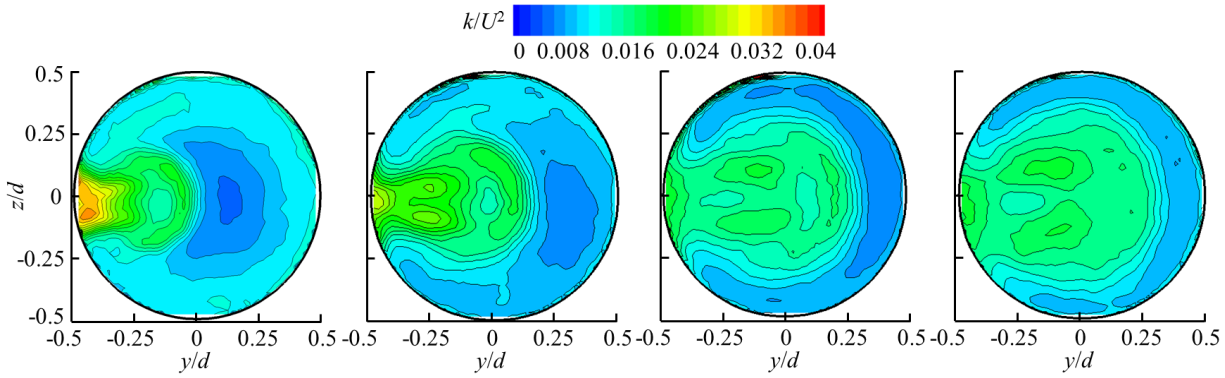

(a) x/d=0.5 (b) x/d=1 (c) x/d=2 (d) x/d=3

Fig. 2.10 Cross-sectional turbulence energy contours downstream of elbow

2.3.5. Axial variation of mass transfer coefficient in and downstream of elbow

Figures 2.11(a)-(c) show the axial variations of mass transfer coefficients in and downstream of the elbow on the inner wall (a), outer wall (b) and side wall (c), respectively. It should be mentioned that the present result of mass transfer coefficient downstream of elbow is evaluated from the plaster dissolution method by axially traversing the laser displacement sensor, while some of the mass transfer coefficients in the elbow are taken from the cross-sectional distributions in Figs. 2.6 and 2.8, where the laser displacement sensor is traversed in radial direction. These results indicate that the mass transfer coefficients taken from two different measurements are in close agreement with each other, which supports the accuracy of mass transfer measurements in the present experiment.

The mass transfer coefficient on the inner wall (Fig. 2.11(a)) decreases immediately after the inlet of the elbow in the first half of the elbow and it increases in the second half of the elbow, and then it decreases gradually in the straight section downstream of the elbow. On the other hand, the mass transfer coefficients on the outer wall (Fig. 2.11(b)) remain almost constant in the elbow, while the mass transfer coefficient on the outer wall decreases slightly downstream of the elbow and increases gradually further downstream of the straight section. The mass transfer coefficients on the side walls of the elbow (Fig. 2.11(b)) stay almost constant K/K_0=1.2 in the elbow, while a minor increase appears in the straight pipe section downstream of the elbow. These results indicate that the influence of the secondary flow on the mass transfer appears in the elbow and it remains in the following straight section more than 3d downstream. Thus, the mass transfer coefficient slowly approaches the axisymmetric distribution downstream of the elbow.

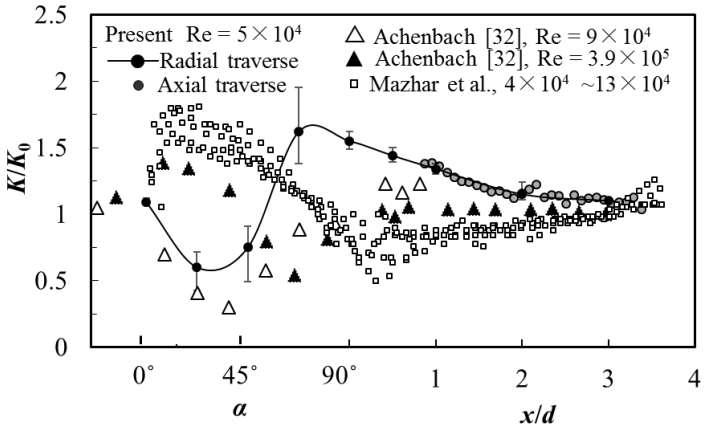

(a) Inner wall

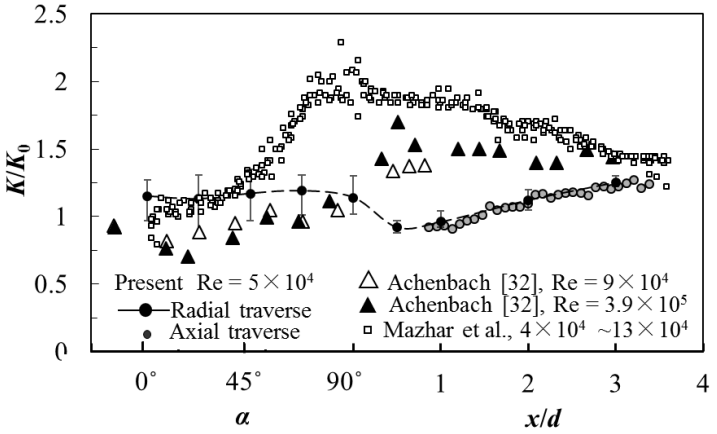

(b)Outer wall

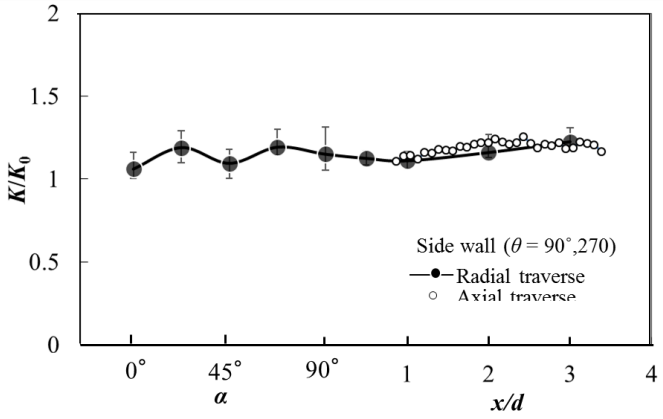

(c) Side wall

Fig. 2.11 Axial variation of mass transfer coefficients in and downstream of elbow

The mass transfer coefficient distributions in a 90° elbow with the radius to pipe diameter ratio 1.5 have been measured in the literature (Achenbach 1976, Mazhar et al. 2013). The experiment by Achenbach (1976) was carried out by working fluid of air at Reynolds number $Re=9\times10^4$ and 3.9×10^5 and at Schmidt number Sc=2.53, while that by Mazhar et al. (2013) was done by the working fluid of water at $Re=(4\text{-}13)\times10^4$ and at Sc=1280. Note that the result by Mazhar et al. (2013) shows a consistent result independent of the Reynolds numbers in the range of experiment. These results of mass transfer distributions are plotted in Fig. 2.11 for comparison. The results of two different Reynolds numbers by Achenbach (1976) show the variation of mass transfer coefficient distribution with the Reynolds number of the flow through the elbow. The measurement in low Reynolds number $Re=9\times10^4$ by Achenbach (1976) shows that the low mass transfer coefficient is observed on the first half of the inner wall of the elbow followed by the high mass transfer coefficient in the second half of the inner wall. This is similarly observed in the present experiment, but the present result shows highest mass transfer coefficient in the second half of the elbow. On the other hand, the experiment by Achenbach (1976) at high Reynolds number ($Re= 3.9\times10^5$) shows a growth of mass transfer coefficient in the first half of the inner wall followed by the decreases in the downstream. The lowest mass transfer coefficient occurs in the second half of the inner wall, which suggests the change of the flow structure in the elbow by the influence of the Reynolds number. A similar feature of mass transfer coefficient at high Reynolds number was observed in the result by Mazhar et al.(2013), in spite of relatively lower Reynolds numbers of their experiments $Re=(4\text{-}13)\times10^4$. The reason why the result by Mazhar et al.(2013) shows the feature of high Reynolds number flow is due to the influence of surface roughness of the experiment as they suggest. On the

other hand, the mass transfer coefficient in the outer wall by Achenbach (1976) at high Reynolds number and Mazhar et al. (2013) similarly shows a gradual increase in the second half of elbow, while the mass transfer coefficient in the present experiment is roughly constant in the outer wall of the elbow, which is followed by a minor decrease downstream of the elbow and the slight increase downstream. These features of the present experiment on the outer wall are deviated from those of mass transfer coefficient of Achenbach (1976) and Mazhar et al. (2013), but a closer agreement can be observed in the mass transfer coefficient distribution by Achenbach at low Reynolds number $Re=9\times10^4$. Therefore, the present mass transfer coefficient distributions in the elbow can be categorized into low Reynolds number flow. Further study on the mass transfer characteristics is needed for clarifying the influence of Reynolds number and Schmidt number to characterize the complex nature of the mass transfer coefficient distribution in a 90° elbow.

2.4. Conclusion

Mass and momentum transfer in and downstream of a 90° long elbow with the radius to diameter ratio 1.5 is studied experimentally using the plaster dissolution method, surface flow visualization and stereo particle image velocimetry at a moderate Reynolds number $Re = 5 \times 10^4$. The results can be summarized as follows:

(1) The mass transfer measurement in the elbow indicates that lower mass transfer coefficients are found in the first half of the inner wall and it increases in the second half of the inner wall, which is followed by the gradual decrease in the downstream.

(2) These features of the mass transfer characteristics in the elbow are highly correlated with the surface flow pattern on the elbow obtained from the oil film method, which

shows a flow convergence in the first half of the inner wall followed by the flow separation in the second half of the inner wall. These results indicate that the variations of mass transfer coefficient in the elbow are highly correlated with the surface flow pattern driven by the flow separation and the secondary flow in the elbow.

(3) The comparative study on the mass transfer, mean velocity and turbulence energy is carried out downstream of the elbow. The low mass transfer coefficient is observed in the first half of the inner wall and it increases in the second half of the inner wall of the elbow, while the mass transfer coefficient stays almost constant on the outer and side walls.

(4) The corresponding variation of the cross sectional mean velocity and turbulence energy shows the generation of secondary flow from the inner to outer wall through the center of the pipe and the return flow from the outer to the inner wall along the side walls of the elbow. The production of high turbulence energy can be expected on the second half of the inner wall, which is due to the combined influence of flow convergence and separation in the elbow. Thus, the mass transfer measurements in the elbow are consistent with the surface flow visualization and velocity field measurements in and downstream of the elbow.

References

Achenbach, E., Mass transfer from bends of circular cross section to air, Future Energy Production Systems, Vol.1, Academic Press, New York, 1976, pp. 327-337.

Anwar, M., So, R.M.C., Swirling turbulent flow through a curved pipe, Exp. Fluids, 14(1993), 85-96.

Enayet, M.M., Gibson, M.M., Taylor, A.M.K.P., Yianneskis, M., 1982. Laser-doppler measurements of laminar and turbulent flow in a pipe bend. Int. J. Heat Fluid Flow. 3, 213-219.

Funatani, S., Fujisawa, N., Simultaneous measurement of temperature and three velocity components in planar cross-section by liquid crystal thermometry combined with stereoscopic particle image velocimetry, Meas. Sci. Technol. 13(2002), 1197-1205.

Iwamoto, Y., Minamiura, H., Sogo, M., Yamano, H., 2010. LDV measurements of a flow in a strongly-curved elbow under a high Reynolds number condition. Trans. Japan Soc. Mech. Eng. 76, 830-838. (in Japanese)

Kiuchi, M., Fujisawa, N., Tomimatsu, S., Performance of PIV system for combusting flow and its application to spray combustor model, J. Vis. 8(2005), 269-276.

Mazhar, H., Ewing, D., Cotton, J.S., Ching, C.Y., Experimental investigation of mass transfer in 90° pipe bends using a dissolvable wall technique, Int. J. Heat Mass Transfer 65(2013), 280-288.

Raffel, M., Willert, C.E., Kompenhans, J., Particle Image Velocimetry, A Practical Guide, Springer, 1998, 174-184.

Yuki, K., Hasegawa, S., Sato, T., Hashizume, H., Aizawa, K., Yamano, H., 2011. Matched refractive index visualization of complex flow structure in a three dimensionally connected dual elbow. Nucl. Eng. Des. 241, 4544-4550.

Chapter 3

Influence of Elbow Curvature on Flow and Turbulence Structure

3.1. Introduction

In this chapter, the influence of the radius ratio of an elbow on the flow and turbulence characteristics was studied by measuring the mean and fluctuating properties of the flow through the elbow at three different radius ratios (r/d = 1.0, 1.2, and 1.5) using planar PIV measurement. Furthermore, the secondary flow characteristics of the elbow were examined by measuring the cross-sectional velocity field near the elbow outlet using stereo PIV, and the results were examined by proper orthogonal decomposition (POD) analysis to understand the variation of turbulence structure by the influence of radius ratio of the elbow.

3.2. Experimental Apparatus and Procedures

3.2.1 Experimental setup

An experimental study on the flow through an elbow was carried out in a closed-circuit water tunnel (Fujisawa et al., 2012). A schematic layout of the tunnel is shown in Fig. 3.1. It consisted of a pump, reservoir tank, honeycomb, flow-developing pipe section, and test section of the elbow, where the measurements of the velocity field were carried out using planar and stereo PIV. It should be noted that the length of

straight circular pipe upstream of the elbow was set to 24*d*, where *d* is the pipe diameter of 56 mm. In the experiment, the ratio of elbow radius *r* to diameter *d* was set to *r/d* = 1.0, 1.2, and 1.5, and the Reynolds number Re (= *Ud/v*) was kept at 3×10^4, 5×10^4, and 10×10^4 for each radius ratio, where *U* is the bulk velocity and *v* is the kinematic viscosity of water. The flow rate of the working fluid (water) was controlled by an inverter of the pump and measured by a digital flow meter. The temperature of the working fluid was kept constant at 303K during the experiment and was achieved by a heating unit with a temperature controller in the reservoir tank.

The test elbow was made of an acrylic resin material for flow visualization purposes, while separating it into two half pipes. Two test elbows were prepared: one was for calibration of the refractive index effect of the elbow, to compensate for image distortion in the velocity measurement, and the other was for measurement of the velocity field in the plane of elbow curvature. Each test elbow was separated into two half pipes in the plane of elbow curvature and in a plane normal to the elbow curvature. The half-pipe structure, separated in the plane of elbow curvature, allowed the insertion of a calibration sheet between them, which was used for calibration of the positions of target images. It should be mentioned that the top surface of the half-pipe structure was flat to minimize the influence of the refractive index difference between the acrylic resin material and working fluid.

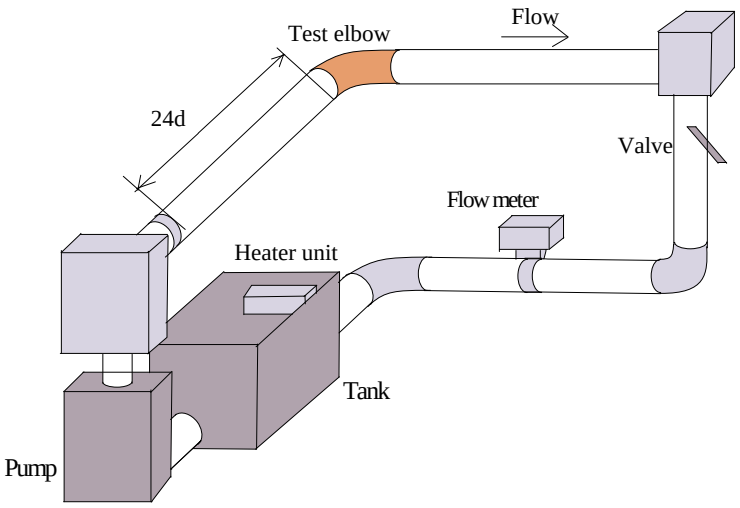

Fig. 3.1 Experimental setup.

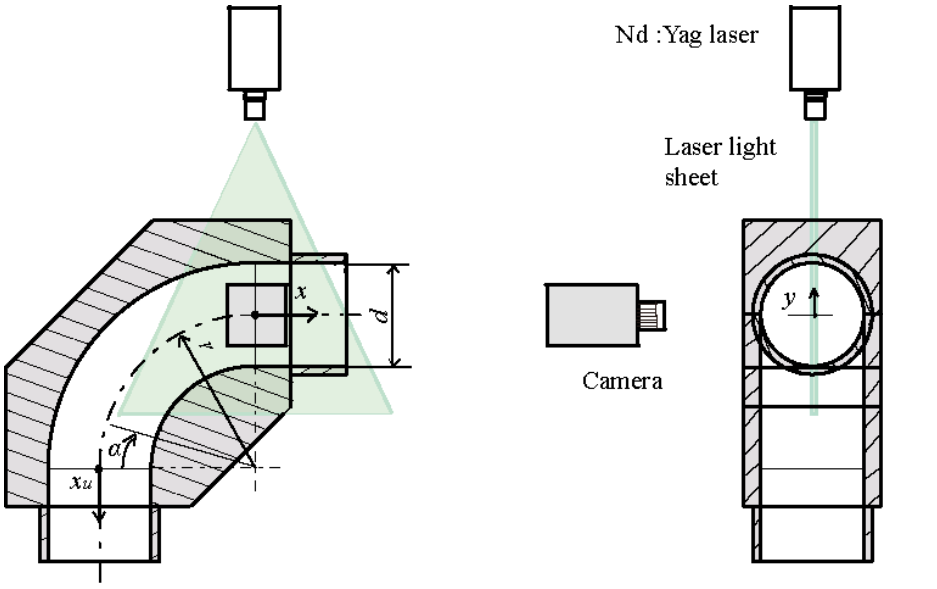

(a)Top view (b) View from downstream

Fig. 3.2 Details of experimental test section.

3.2.2 Measurement of velocity field by PIV

The velocity field in the plane of elbow curvature was measured by a planar PIV system, as shown in Fig. 3.2. It consisted of a CCD camera with a frame-straddling

function (1018 × 1008 pixels with 8 bits of gray levels), double-pulsed Nd:YAG lasers (maximum output energy 70 mJ/pulse), and pulse controller. Light sheet illumination for flow visualization was provided from the side of the test section. The thickness of the light sheet was about 1 mm. The flow visualization was carried out using nylon tracer particles of 40 μm in diameter and a specific gravity of 1.02, which were supplied to the water from a reservoir tank located upstream of the pump.

To characterize the mean and fluctuating velocities in the elbow, planar PIV measurements were carried out through the test elbow. For this to be done, the image deformation by the refractive index difference at the interface of wall material and working fluid water is a major source of uncertainty of measurement. In this study, the image deformation was corrected by theoretically with the relative refractive index of the wall material and working fluid water, which is described in Appendix A. Furthermore, the uncertainty of the theoretical correction is estimated in comparison with the experimental calibration technique located across the elbow section (For details see Appendix A).

The velocity field in the cross-sectional plane downstream of the elbow was measured by the stereo PIV system, which is illustrated in Fig. 3.3. During the measurement, the cross section downstream of the elbow outlet at x/d = 0.5 was illuminated by a light sheet from pulsed Nd:YAG lasers. Then, flow images were taken by two CCD cameras located on each side of the test section, with an inclination angle of ±45 degrees based on the Scheimpflug configuration. The stereo PIV system allowed measurement of the three-dimentional velocity field in the cross section of interest through water jackets on both sides of the pipe. The flow observation was carried out through the water jackets to minimize the influence of the refractive index difference at

the interface of the test elbow and working fluid. It should be noted that the front surface of each water jacket was made normal to the camera axis to minimize the effect of the above-mentioned refractive index difference.

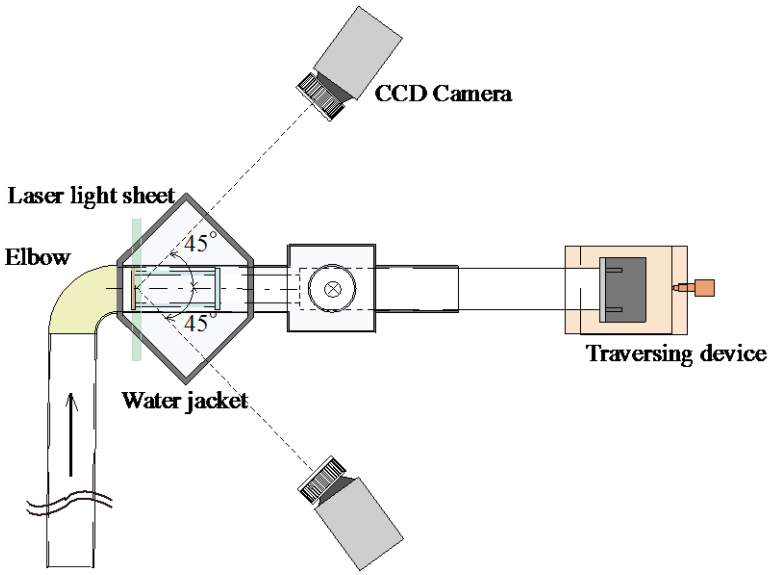

Fig. 3.3 Experimental arrangement of stereo PIV system.

Image distortions were calibrated using a 53-mm diameter circular calibration plate, on which a grid-line pattern with 2.5 mm intervals was drawn using a 0.5-mm line width. The calibration plate was traversed axially using a mechanical traversing gear that was driven manually with an accuracy of 5 μm. Then, a total of five images were captured axially in 0.5-mm increments. These images were used for the three-dimentional calibration of the stereo PIV, in which the analysis was carried out between two sequential images using a direct cross-correlation algorithm with a sub-pixel interpolation technique (Kiuchi et al., 2005). Next, the particle displacements from each camera were combined to produce three-dimentional velocity vectors by

solving the system equations for the stereo cameras using a least-square method (Funatani and Fujisawa, 2002).

The PIV analysis of the planar and stereo PIV images were carried out using a direct cross-correlation algorithm. The interrogation window size was set to 31 × 31 pixels with a 50% overlap in the analysis. Note that the interrogation window size was found optimal from the number of invalid velocity vectors, because the uncertainty interval decreases with increasing the interrogation window size, while the spatial resolution decreases (Wieneke 2015). The statistical properties of the mean and fluctuating velocities were evaluated from 500 instantaneous velocity fields measured in time intervals of 1/5 of a second. The maximum pixel displacement of the particle images was set to about four pixels in the velocity measurement by tuning the time interval of two sequential images for PIV. Note that the number of invalid velocity vectors was less than 1% of the total analyzed velocity vectors.

The uncertainty of velocity measurement by planar PIV was estimated at the elbow centerline using the PIV uncertainty quantification by Wieneke (2015). It is noted that the out-of-plane velocity is estimated as 20% of the mean velocity, seeding density 0.09 and particle diameter 2 pixels, which result in errors of 0.1 pixels, 0.075 pixels and 0.05 pixels, respectively. The total uncertainty interval of velocity measurement is 3.4%. However, the uncertainty is increased due to the image deformation error in radial direction caused by the influence of refractive index difference between the acrylic material and working fluid water, which is 3.8% of the uncertainty at 95% confidence level (See Appendix A). Therefore total uncertainty interval of velocity measurement was estimated 4.9% at 95% confidence level.

To evaluate the cross-sectional flow structure downstream of the elbow, POD analyses were introduced into the stereo PIV data of the 500 instantaneous velocity fields in the cross-sectional plane downstream of the elbow outlet. The basic idea of snapshot POD is that it yields a set of orthogonal eigenfunctions that are optimal in energy, representing the temporal and spatial correlations of the instantaneous velocities (Berkootz et al., 1993; Bernero, 2000; Kostas, 2005; Fujisawa, 2015). A POD analysis allows an evaluation of the mean velocity field (0^{th} POD mode) and fluctuating velocity field (1^{st}, 2^{nd}, etc.), where the numbering is arranged in descending order of fluctuating energy and is made dimensionless by the total fluctuating energy of the radius ratio r/d = 1.0. The details of snapshot POD analysis have been described in the literature (Fujisawa et al., 2015).

3.3. Results and Discussion

To complete as the database of the flow through elbows, the mean and fluctuating velocity upstream x_u/d= 2 of the elbow were measured by stereo PIV, and the results are summarized in Appendix B.

3.3.1 Mean flow characteristics in elbow

Figures 3.4 and 3.5 show the axial and wall-normal mean velocity distributions, respectively, at eight cross sections along the test section. They include the cross sections upstream of the elbow (x_u/d = 1), those in the elbow (elbow angle α = 0°, 22.5°, 45°, 67.5°, and 90°), and those downstream of the elbow (x/d = 0.5, 1). The present results of the axial mean velocity distribution upstream of the elbow (Fig. 3.4) show a developed profile, whereas the wall-normal mean velocity (Fig. 3.5) shows a negligibly small velocity upstream of the elbow, suggesting the soundness of the present measurement. When the measuring position moves into the elbow section, the axial

mean velocity distribution changes quickly (α = 0°). The mean velocity increases near the inner wall and decreases near the outer wall. This is caused by the effect of the pressure gradient at the inlet of the inner wall, as described by Sudo et al. (1998). It should be noted that the velocity difference between the inner and outer walls contributed to the occurrence of a secondary flow in the cross section of the elbow. With an increase in the elbow angle to α = 22.5°, the near-wall axial velocity increased more on the inner wall and that decreased on the outer wall, which resulted in the growth of a negative velocity gradient across the elbow. On the other hand, the wall-normal mean velocity decreased because of the following reduction in the mean velocity gradient normal to the wall. With an increase in elbow angle to α = 45°, the near-wall axial velocity starts decreasing on the inner wall and increasing on the outer wall, which is the opposite effect observed at small elbow angles from α = 0° to 22.5°. Therefore, the flow behavior changes at the angle α = 45°, where the flow moves away from the inner wall, as seen in the wall-normal velocity distribution in Fig. 3.5. It should be noted that the influence of the radius ratio is not so clearly observed up to the elbow angle α = 45°, which is the flow characteristic in the first half of the elbow. With further increases in the elbow angle to α = 67.5°, the near-wall velocity decreases on the inner wall, the flow separation occurs, and the influence of the radius ratio appears near the inner wall. This result indicates that the separation point on the inner wall changes with the variation in radius ratio. It is found that the velocity profile becomes lean as the radius ratio decreases, so that earlier separation can occur for elbows with smaller radius ratios. Further downstream at α = 90°, the near-wall velocity distribution shows a clear indication of the radius ratio, where reverse flow appears in the short elbow (r/d = 1.0), whereas the flow is not fully separated in the middle elbow (r/d = 1.2) and long elbow

(r/d = 1.5). The low-velocity region near the inner wall grows up to 1/4 of the elbow diameter, and this region increases with increasing downstream distance. The negative velocity gradient across the elbow is weakened at this elbow angle (α = 90°) by the occurrence of a low-velocity region on the inner wall. Therefore, the secondary flow across the elbow is weakened near the elbow outlet. It should be mentioned that the wall-normal mean velocity is highly promoted in the middle of the elbow, reflecting the occurrence of flow separation on the inner wall. Downstream of the elbow ($x_d = 1d$), the low-velocity region near the inner wall grows normal to the inner wall and extends beyond the elbow centerline. The low-velocity region near the inner wall recovers downstream of the elbow, and the wall-normal mean velocity decreases with increasing downstream distance. It should be noted that the velocity distributions downstream of the elbow show the influence of the radius ratio, as was observed in the second half of the elbow. On the other hand, the flow over the outer wall shows a gradual increase along the wall except for a minor decrease at the elbow inlet (α = 0°). This is mainly due to the change of pressure gradient across the outer wall, whereas the influence of the radius ratio is not clearly observed on the velocity distribution on the outer wall compared with that on the inner wall. This was due to the presence of an attached flow on the outer wall, which was in contrast with the separated or near-separated flow on the inner wall.

The mean velocity distributions in the elbow were measured by Iwamoto et al. (2010) for a short elbow (r/d = 1.0) and by Mazhar et al. (2016) for a long elbow (r/d = 1.5). These are shown in Fig. 3.4 for comparison purposes. The mean velocity distribution upstream of the elbow inlet shows a certain deviation owing to the influence of the flow-developing length, which is 10d in Iwamoto et al. (2010), 63d in Mazhar et

al. (2016), and 24d in the present experiment. It can be seen that the present result agrees more closely with Iwamoto et al. (2010) than with Mazhar et al. (2016), reflecting the influence of the flow-developing length. Therefore, the mean velocity distribution in the elbow can be affected by the initial mean velocity distributions, as observed from the results of elbow angle α=45° by Mazhar et al. (2016), whereas the results of Iwamoto et al. (2010) are much closer to the present result. It should be mentioned that the general features of mean velocity variation in the elbow in the present measurements are consistent with those of Iwamoto et al. (2010), Mazhar et al. (2016), and Taguchi et al. (2018). It should be noted that the results by Taguchi et al. (2018) were obtained using the same experimental apparatus, so they agree closely with the present results for a long elbow (r/d = 1.5).

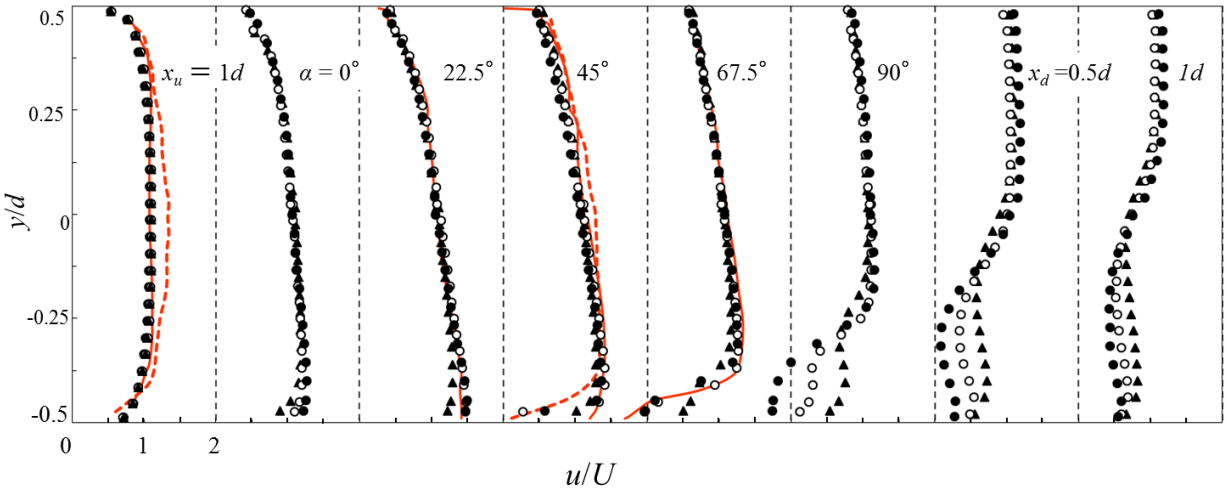

Fig. 3.4 Streamwise mean velocity distribution in and downstream of the elbow for three radius ratios (●: r/d = 1.0, ○: r/d = 1.2, ▲: r/d = 1.5, ———: Iwamoto et al. (2010), - - - - -: Mazhar et al. (2016)) Re = 5×10^4.

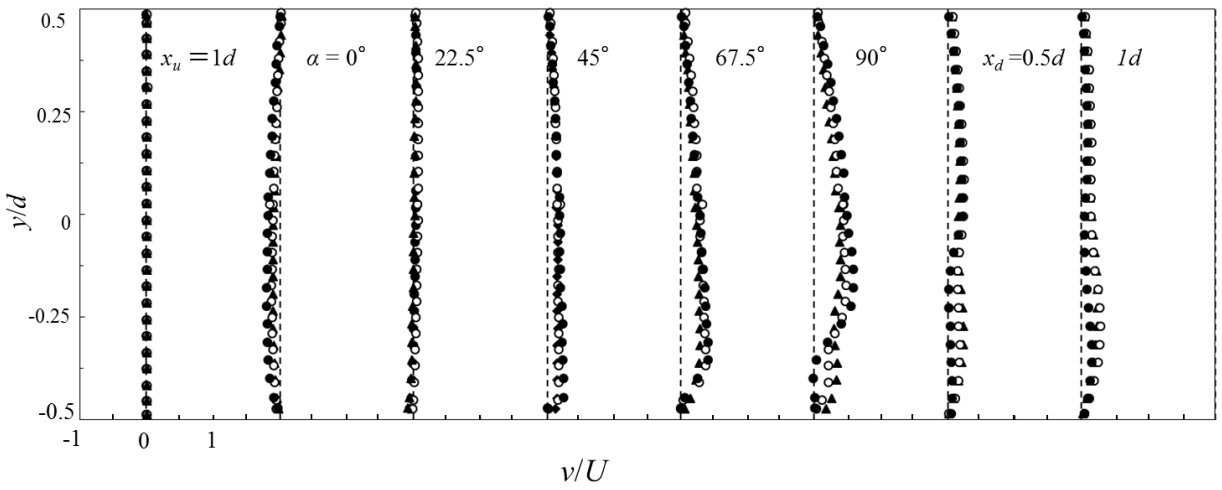

Fig. 3.5 Wall-normal mean velocity distribution in and downstream of the elbow for three radius ratios (●: *r/d* = 1.0, ○: *r/d* = 1.2, ▲: *r/d* = 1.5) Re = 5×10^4.

Figures 3.6 and 3.7 show the axial and wall-normal mean velocity distributions in the test section, respectively, for a short elbow (*r/d* = 1.0). Each figure shows the experimental results at different Reynolds numbers Re = 3×10^4, 5×10^4, and 10×10^4, which allow understanding of the Reynolds number effect on the flow field in a short elbow. The effect on the mean velocity distribution appears in the second half of the elbow (α = 45 to 90°) and persists further downstream. Although the flow near the inner wall indicates a flow separation at lower Reynolds numbers, it is not likely to occur on the inner wall at higher Reynolds numbers such as Re = 10×10^4. This is because the secondary flow in the elbow is weakened at higher Reynolds numbers. However, this result does not apply to a long elbow (*r/d* = 1.5), where the mean flow and turbulence characteristics do not change with variations in Reynolds number (Taguchi et al., 2018). Similarly, the wall-normal velocity distribution (Fig. 3.7) shows an effect of the

Reynolds number in the second half of the elbow, but it is smaller than that of the axial mean velocity distribution. These results indicate that the mean velocity field in the elbow is modified not only by the radius ratio but also by the Reynolds number.

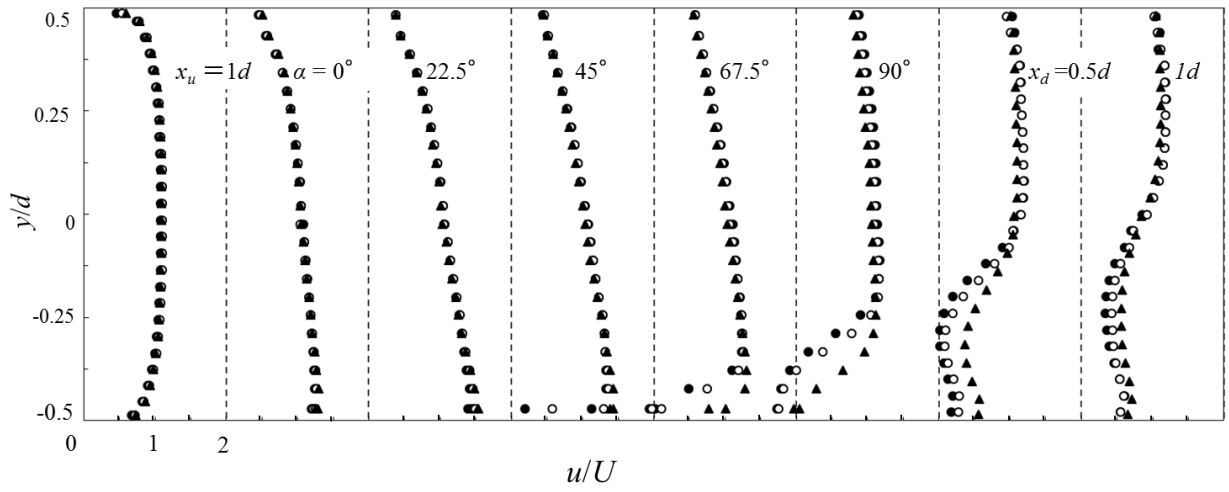

Fig. 3.6 Streamwise mean velocity distribution in and downstream of the elbow for three Reynolds numbers (●: Re = 3×10^4, ○: Re = 5×10^4, ▲: Re = 10×10^4).

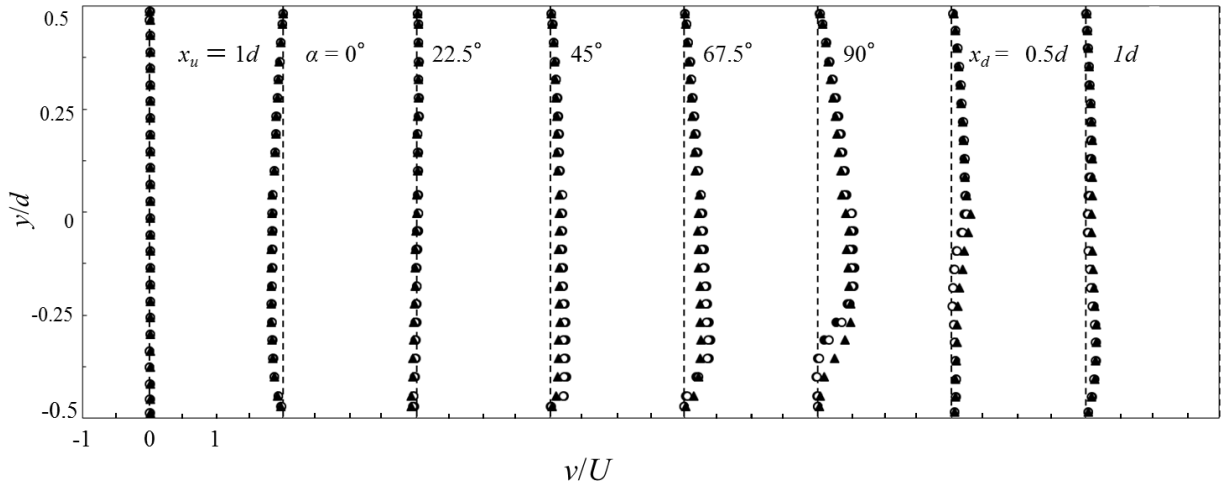

Fig. 3.7 Wall-normal mean velocity distribution in and downstream of the elbow for three Reynolds numbers (●: Re = 3×10^4, ○: Re = 5×10^4, ▲: Re = 10×10^4).

3.3.2 Turbulence characteristics in an elbow

Figures 3.8 and 3.9 show the cross-sectional distributions of axial and wall-normal turbulence intensities, respectively, for various positions of the test section, in the straight pipe upstream (x_u/d= 1), in the elbow section (α = 0°, 22.5°, 45°, 67.5°, 90°), and in the straight pipe downstream (x/d = 0.5, 1). The experimental results (Fig. 3.8) show that the axial turbulence intensity increases along the inner wall as the flow approaches the elbow outlet, whereas that on the outer wall stays at roughly the same magnitude as the elbow inlet. A minor change in the axial turbulence intensity distribution occurs in the first half of the inner wall (α = 0 to 45°), whereas an apparent increase occurs in the second half (α = 45 to 90°) and the local peak moves away from the wall with increasing downstream distance. Although the behavior of the turbulence intensity on the inner wall is similar for the three elbows, the peak magnitude of the turbulence intensity increases with decreasing radius ratio. This result is closely related to the variation in mean velocity gradient near the inner wall, because the generation of turbulence intensity is highly dependent on the mean velocity gradient. Therefore, the turbulence intensity in the short elbow (r/d = 1.0) is highest on the second half of the inner wall, followed by that of the middle elbow (r/d = 1.2) and long elbow (r/d = 1.5). On the other hand, the wall-normal turbulence intensity in Fig. 3.9 behaves similar to the axial turbulence intensity distribution in Fig. 3.8, although the growth rate of the wall-normal turbulence intensity is rather small compared with that of the axial turbulence intensity. It should be noted that the wall-normal turbulence intensity decreases with proximity to the wall, reflecting the near-wall damping effect of the turbulence. On the other hand, the axial turbulence intensity on the outer wall remains at the same magnitude as that of the elbow inlet, while the wall-normal turbulence

intensity on the outer wall grows in the elbow section. This is reflected by the formation of unstable flow on the outer wall against the centrifugal forces, as was observed in the mean velocity distribution in Fig. 3.4. It should be noted that the downstream variations in axial turbulence intensity by Iwamoto et al. (2010) are well reproduced in the present measurements. However, the magnitude of the axial turbulence intensity is slightly smaller than the present measurements, reflecting the effect of a shorter developing length upstream of the elbow.

Figure 3.10 shows the Reynolds stress distributions along the test section of the elbow at various positions upstream and downstream of the elbow. The Reynolds stress distributions in the first half of the elbow do not indicate a clear change of distribution near the inner wall of the elbow, which is similar to the turbulence intensity distributions in Figs. 3.8 and 3.9. However, there is a small growth of the Reynolds stress magnitude, which is reflected by the local growth of the wall-normal turbulence intensity on the outer wall in Fig. 3.9. It can be seen that a negative Reynolds stress is generated on the inner wall at elbow angle α = 67.5°, which is followed by the formation of a positive Reynolds stress near the wall at elbow angle α = 90°. The occurrence of negative Reynolds stress is an indication of the formation of flow separation on the inner wall of the elbow. In the downstream portion of the elbow, the positive Reynolds stress increases away from the inner wall and the peak position also moves away from the wall. It should be noted that the Reynolds stress distribution is modified by the radius-ratio effect, which is evident in the second half of the short elbow (r/d = 1.0), followed by a decrease in the middle elbow (r/d = 1.2) and long elbow (r/d = 1.5). These results indicate that the flow in the second half of the inner wall of the short elbow is highly turbulent because of the presence of flow separation. It

should be mentioned that a negative Reynolds stress appears in the second half of the elbow, but its sign changes around the elbow outlet and becomes positive downstream, reflecting the formation of a separating flow near the elbow outlet.

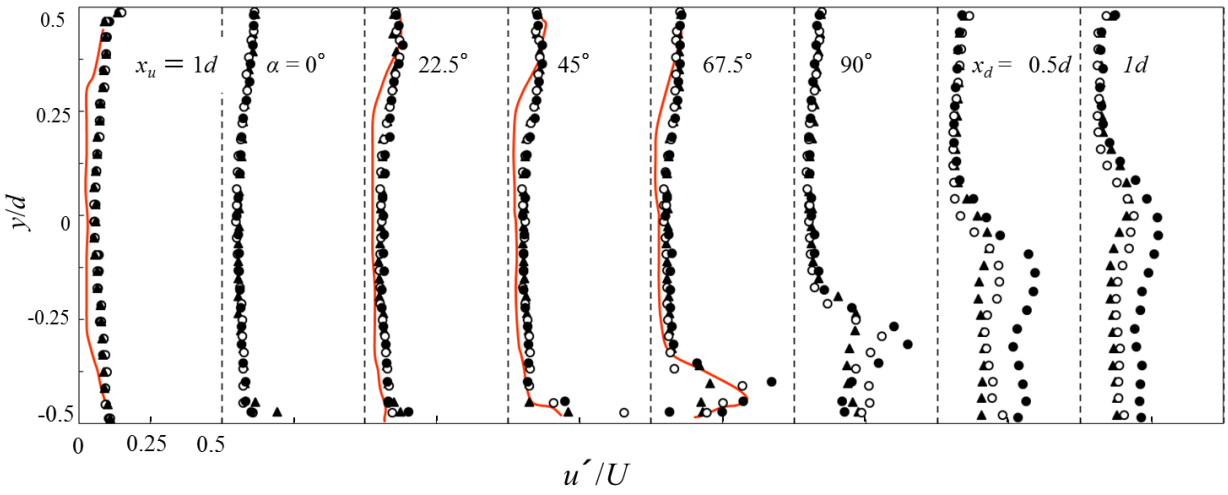

Fig. 3.8 Axial turbulence intensity distribution in and downstream of the elbow for three radius ratios (●: r/d = 1.0, ○: r/d = 1.2, ▲: r/d = 1.5, ——— : Iwamoto et al. (2010)) Re = 5×10^4.

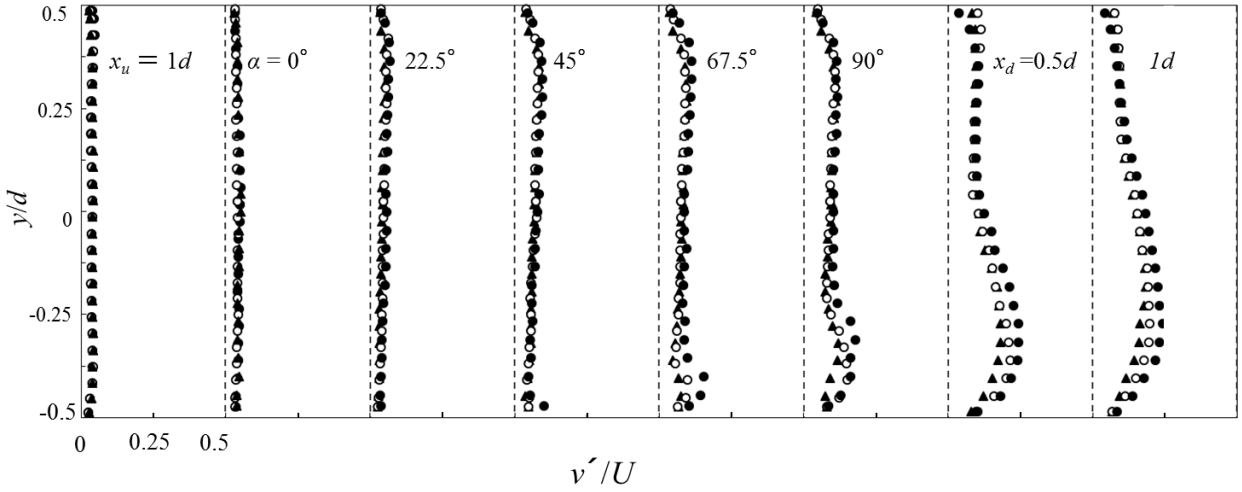

.

Fig. 3.9 Wall-normal turbulence intensity distribution in and downstream of the elbow for three radius ratios (●: r/d = 1.0, ○: r/d = 1.2, ▲: r/d = 1.5) Re = 5×10^4.

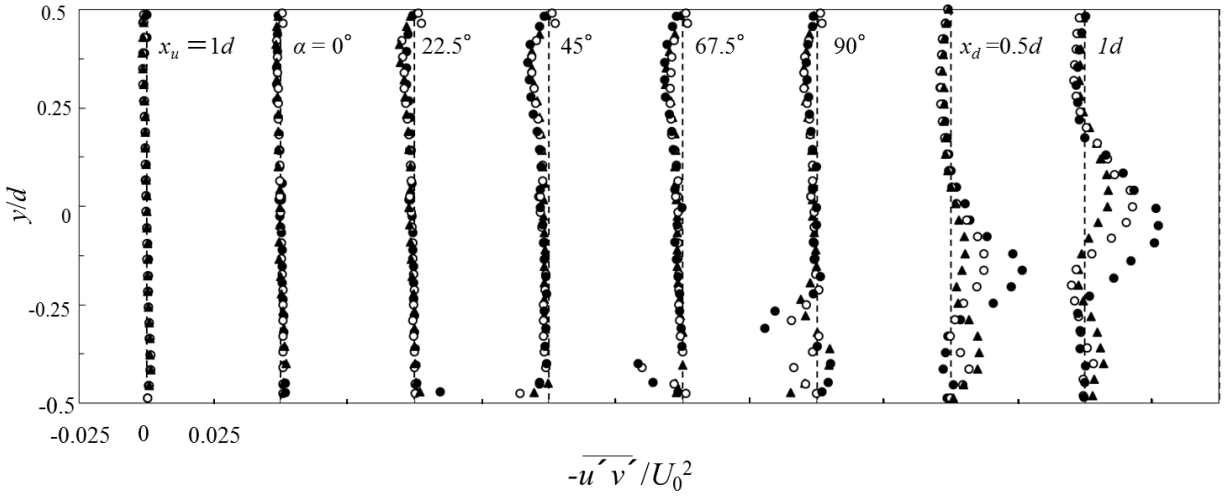

Fig. 3.10 Reynolds stress distribution in and downstream of the elbow for three radius ratios (●: r/d = 1.0, ○: r/d = 1.2, ▲: r/d = 1.5) Re = 5×10^4.

Figures 3.11 and 3.12 show the cross-sectional distributions of axial and wall-normal turbulence intensities, respectively, for three Reynolds numbers (Re = 3×10^4, 5×10^4, and 10×10^4) in the case of the short elbow (r/d = 1.0). These results indicate that the Reynolds number effect is clearly observed in the second half of the inner wall and that it persists downstream. The turbulence intensity starts growing around the angle α = 45°, but the peak position seems to be shifted away from the wall with decreasing Reynolds number. This reflects the variation in mean velocity distribution on the inner wall at higher Reynolds numbers (Fig. 3.4). It should be mentioned that the Reynolds number effect is clearly seen on the axial turbulence intensity but is not so evident on the wall-normal turbulence intensity due to the wall-damping effect (Fig. 3.12). It should be noted that the measurement of turbulence intensities in the long elbow (r/d = 1.5) does not change with Reynolds number (Taguchi et al., 2018), which is different from the present result. This difference arises from the fact that the flow through the short elbow separates on the inner wall owing to

the occurrence of high pressure gradient along the elbow and the position of flow separation may change with Reynolds number. However, the flow separation does not occur clearly for the flow though the long elbow, especially at higher Reynolds number.

Figure 3.13 shows the Reynolds stress distributions along the test section at three Reynolds numbers Re = 3×10^4, 5×10^4, and 10×10^4 in the case of the short elbow (r/d =1.0). The Reynolds stress starts growing at the elbow angle α = 45° and keeps growing in the second half of the elbow. Furthermore, the Reynolds number effect is clearly seen in the second half on the inner wall and is similar to the turbulence intensity distribution in Figs. 3.11 and 3.12.

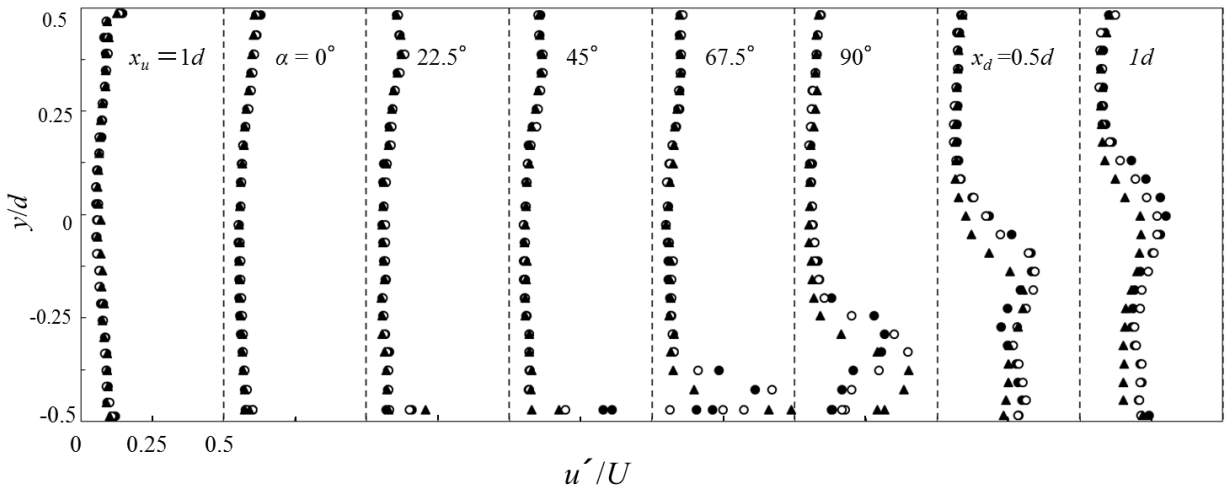

Fig. 3.11 Axial turbulence intensity distribution in and downstream of elbow for three Reynolds numbers (●: Re = 3×10^4, ○: Re = 5×10^4, ▲: Re = 10×10^4).

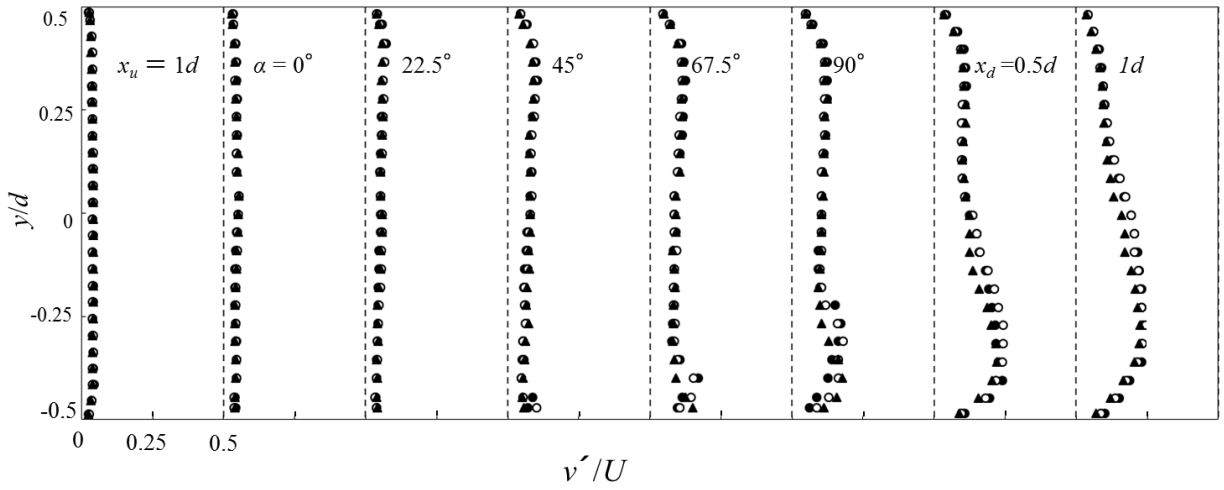

Fig. 3.12 Normal turbulence intensity distribution in and downstream of the elbow for three Reynolds numbers (●: Re = 3 × 10^4, ○: Re = 5 × 10^4, ▲: Re = 10 × 10^4)

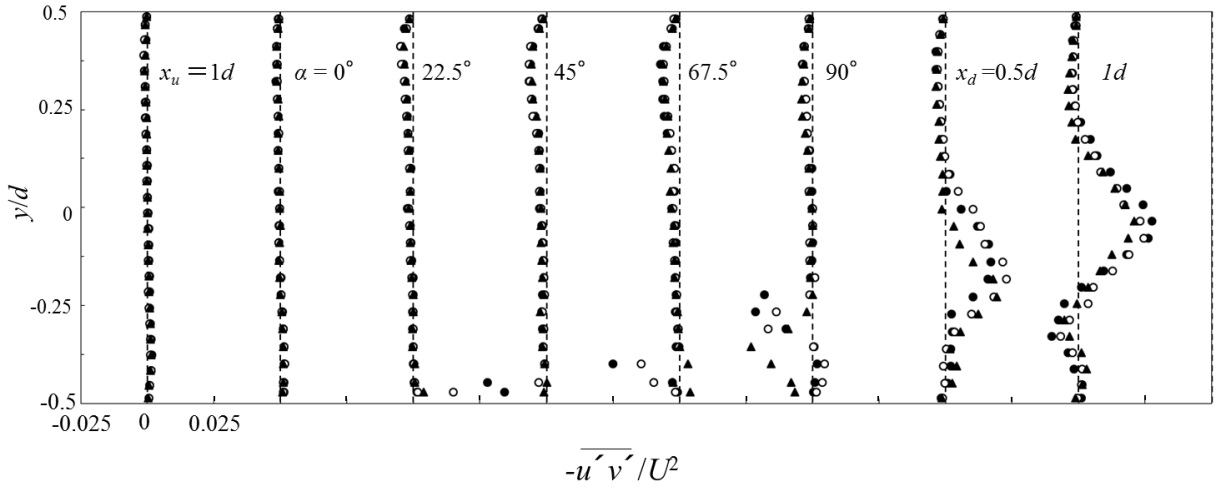

Fig. 3.13 Reynolds stress distribution in and downstream of the elbow for three Reynolds numbers (●: Re = 3 × 10^4, ○: Re = 5 × 10^4, ▲: Re = 10 × 10^4)

3.3.3 Cross-sectional distribution of mean and turbulence characteristics near the elbow outlet

Figure 3.14(a), (b), and (c) shows an example of the instantaneous velocity field in the cross section downstream of the elbow (x/d= 0.5) for three radius ratios r/d = 1.0, 1.2, and 1.5, respectively, which were obtained from the stereo PIV measurements. The in-plane velocities are shown by the velocity vectors, and the axial velocity magnitude is indicated by the color contours. These flow fields indicate that a pair of counter-rotating vortices is generated in the cross section of the elbow and that they are fluctuating in space and time, which is associated with the unsteadiness of the flow field. It can be seen that the counter-rotating vortices stay near the inner wall of the elbow with lower axial velocity than the rest of the cross section. The lowest axial velocity on the inner wall occurs in the short elbow (r/d = 1.0), where flow separation is observed in the mean velocity distribution (Fig.3.4). The magnitude of the lower velocity on the inner wall increases with increasing radius ratio. Therefore, the secondary flow motion in the cross-sectional plane seems to be weakened at larger radius ratios. This phenomenon may correspond with the occurrence of flow separation on the inner wall of the short elbow.

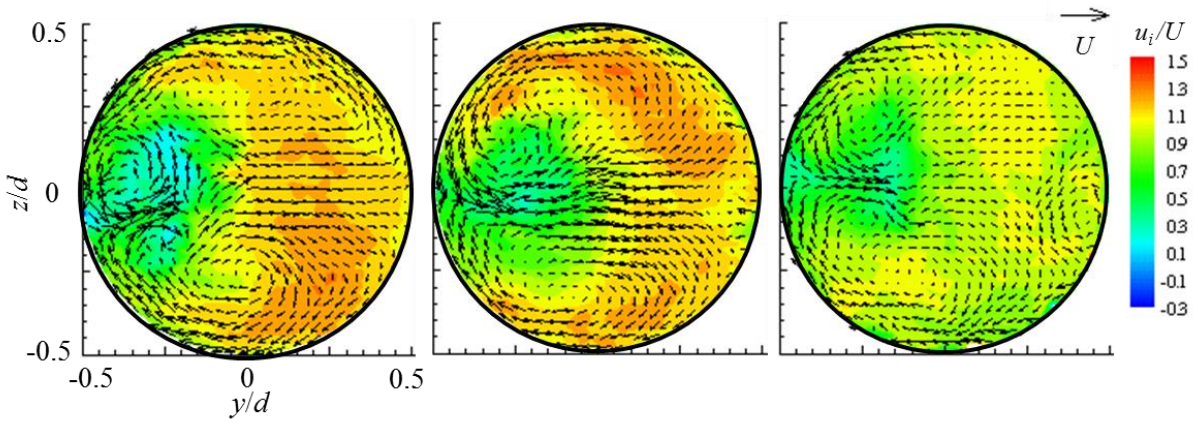

(a) r/d = 1.0 (b) r/d = 1.2 (c) r/d = 1.5

Fig. 3.14 Cross-sectional velocity field near the elbow outlet.

Figures 3.15 and 16 show the cross-sectional mean velocity field downstream of the elbow (x/d = 0.5) for the three radius ratios. The color contour shows the axial mean velocity (Fig. 3.15) and in-plane velocity magnitude (Fig. 3.16), respectively, whereas the in-plane velocity is shown by velocity vectors. The axial mean velocity (Fig.3.15) of the short elbow (r/d = 1.0) shows a lower axial velocity field on the inner wall of the elbow, whereas a higher axial velocity prevails on the outer wall, reflecting the mean velocity distribution across the elbow in Fig. 3.4. It can be seen that the in-plane flow moves away from the inner wall to the outer wall through the pipe centerline. This movement is driven by the centrifugal forces, while the flow on the outer wall moves along the side wall and returns to the inner wall. It should be noted that the in-plane velocity magnitude (Fig. 3.16) is magnified with decreasing radius ratio. This is caused by the secondary flow that is driven by the centrifugal forces, which is strengthened with decreasing radius ratio. Therefore, highly turbulent flow is generated on the inner wall in the short elbow. This is associated with the occurrence of flow separation on the inner wall. On the other hand, secondary flow in the cross section is weakened on both sides of the inner wall and outer wall in the case of middle and long elbows. This is associated with the weakening of the flow separation with increasing radius ratios. Therefore, the secondary flow in the cross section of the elbow outlet is highly modified by the radius ratio effect.

Figure 3.17 shows the contour plots of the axial turbulence intensity downstream of elbow (x/d = 0.5). It is apparent that a highly turbulent region is formed on the inner wall of the short elbow. This is caused by the flow separation on the inner wall, whereas its magnitude and area are decreased in the middle and long elbows. This result coincides well with the flow field observations of the mean velocity (Figs. 3.6, 3.7) and turbulence intensities (Figs. 3.11, 3.12) across the pipe centerline.

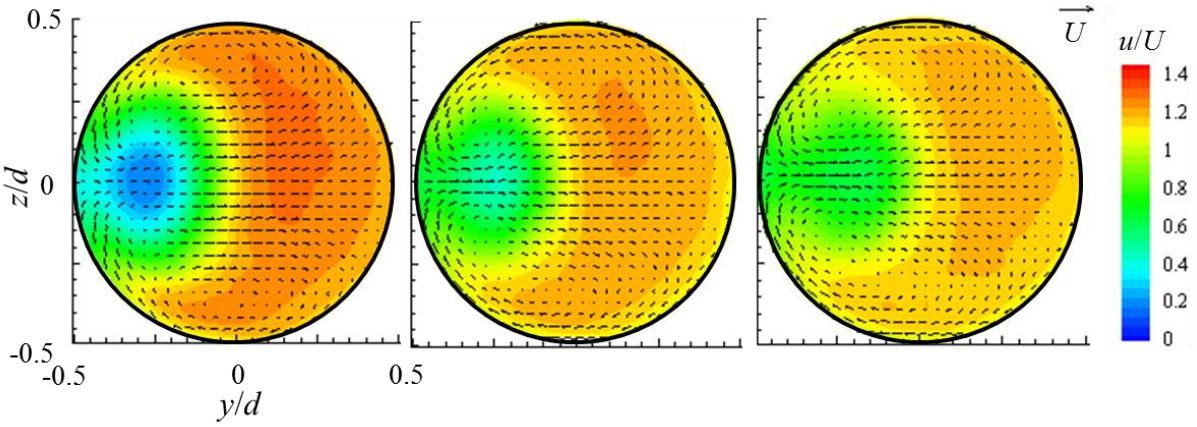

(a) r/d =1.0 (b) 1.2 (c) 1.5

Fig. 3.15 Mean velocity contours near the elbow outlet (x/d = 0.5) Re = 5×10^4.

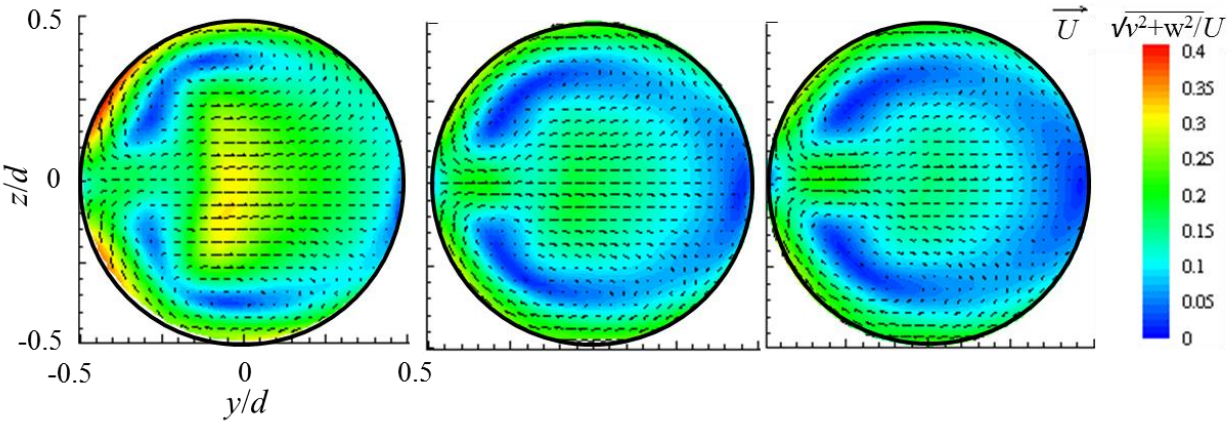

(a) r/d =1.0 (b) 1.2 (c) 1.5

Fig. 3.16 In-plane velocity magnitude contours near the elbow outlet (x/d = 0.5) Re = 5×10^4.

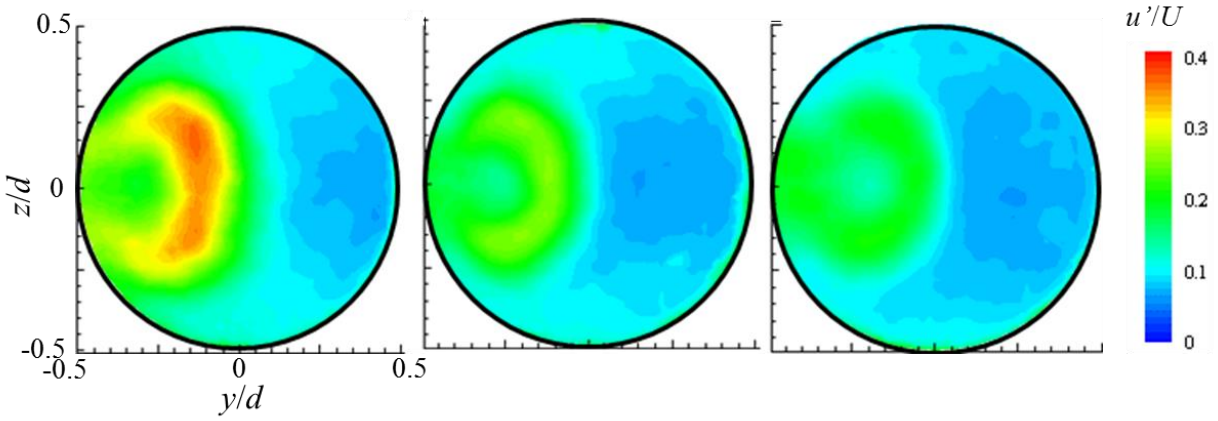

(a) r/d = 1.0 (b) 1.2 (c) 1.5

Fig. 3.17 Axial turbulence intensity contours near the elbow outlet (x/d = 0.5) Re = 5×10^4.

3.3.4 POD analysis of flow structure near elbow outlet

To understand the flow structure of the flow through the elbow, snapshot POD analysis was introduced into the cross-sectional velocity field downstream of a 90° elbow. Figure 3.18 shows the first POD mode of the axial velocity fluctuations downstream of a 90° elbow for the three radius ratios r/d = 1.0, 1.2, and 1.5, respectively, which are obtained from the POD analysis of 500 instantaneous velocity fields taken at five frames per second. It should be noted that the first POD mode contains the highest fluctuating energy levels of all the POD modes, which are 18.3%, 16.6%, and 15.8% of the total fluctuating energy for the radius ratios r/d = 1.0, 1.2, and 1.5, respectively. Note that the fluctuating energy levels of the 2nd and higher POD modes are much smaller than the 1st POD modes, so that only the 1st POD mode is described in Fig. 3.18. The fluctuating energy levels of higher POD modes are shown in Table 3.1. The present results indicate that the opposite sign of the POD mode exists on both sides of the inner wall of the elbow, which corresponds to the alternative flow motion of the counter-rotating vortices on that wall. This is consistent with

Table 3.1 Fluctuating energy level of POD modes

Radius ratio *r/d*	1st POD	2nd POD	3rd POD	4th POD
1.0	18.3 %	7.3 %	5.5 %	4.4 %
1.2	16.6 %	6.6 %	5.7 %	3.8 %
1.5	15.8 %	5.2 %	4.6 %	2.8 %

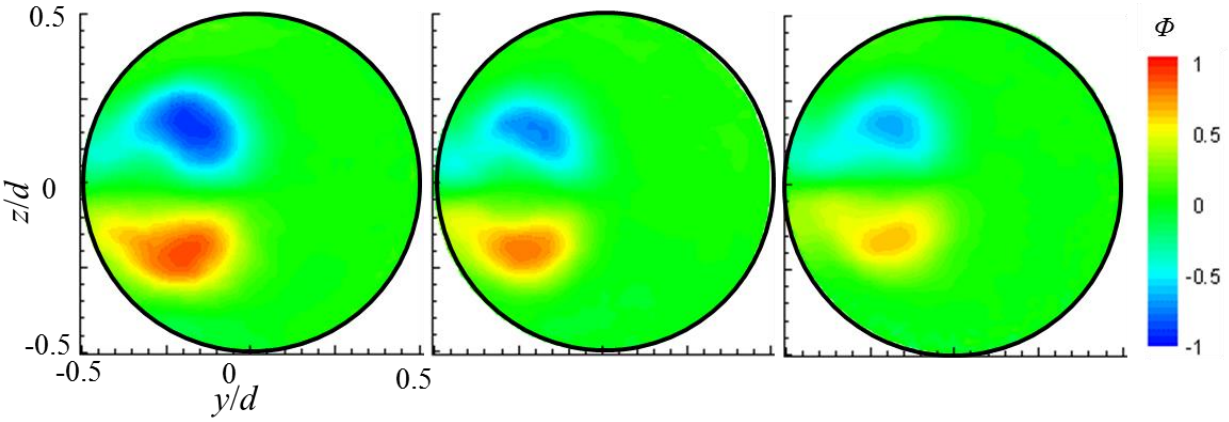

(a) *r/d* =1.0 (b) 1.2 (c) 1.5

Fig. 3.18 First POD mode of axial velocity fluctuations near elbow outlet (*x/d* = 0.5) Re = 5×10^4.

the cross-sectional observations of the secondary flow in Fig. 3.14. It should also be noted that the peak position of the first POD mode is in the region of high turbulence intensity and that it decreases with increasing radius ratio. The decrease in the peak of the first POD mode at higher radius ratios corresponds to a weakening of the highly turbulent flow in the cross section of the elbow, as observed in the axial turbulence intensity contours in Fig. 3.17. When the first POD mode is stronger, it means that it has a greater coherent flow structure which may be less turbulent or more organized by being affected by the geometric characteristics of the elbow.

3.4. Conclusions

The velocity fields in and downstream of a 90° elbow were studied experimentally using planar, stereo PIV measurements to understand the influence of the elbow radius ratios in the range of 1.0 to 1.5 and Reynolds numbers in the range of Re = (3 to 10) × 10^4 on the flow field and turbulence structure. The results are summarized as follows:

1. The experimental results showed that the axial mean velocity decreased along the inner wall in the second half of the elbow and the flow approached separation near the outlet of the inner wall. The turbulence intensity increased along the inner wall, and the secondary flow was highly promoted in the elbow outlet. These effects of the radius ratio were highly promoted in the short elbow, where flow separation occurred near the elbow outlet.
2. A Reynolds number effect appeared on the mean and turbulence characteristics of the elbows with smaller radius ratios. However, the Reynolds number effect was not clearly observed with increasing radius ratio. This effect seemed to be related to the flow separation in the elbow.
3. The in-plane mean velocity contour in the cross-sectional plane of the elbow outlet indicated the presence of a pair of counter-rotating vortices. The in-plane mean velocity magnitude and turbulence energy increased with decreasing radius ratio.
4. A POD analysis showed that a pair of highly correlated regions existed on both sides of the inner wall, which indicated an alternative secondary flow motion in the elbow. The first POD mode contains the major fluctuating energy and the peak increased with decreasing radius ratio. This promoted the secondary flow and resulted in a growth of turbulence energy on the inner wall with decreasing radius ratio.

Appendix A: Image deformation correction and uncertainty

Fig. 3.A-1 shows the illustration of image deformation caused by the refractive index difference between the acrylic wall material and the working fluid water. The deformation distance δ is evaluated from the following equation, which is based on the Snell's law of refraction:

$$\delta = r \cos\theta_i \tan\theta' \qquad \text{(A-1)}$$

where $$\theta' = \sin^{-1}(n_{wa} \sin\theta_i) - \theta_i \qquad \text{(A-2)}$$

r: pipe radius, θ_i: angle of incidence, n_{wa}: relative refractive index of water to acrylic material. Then, the magnification factor M ($=\Delta\delta/\Delta y$) between the planes of measurement $\Delta\delta$ and outside elbow Δy can be evaluated from Eq.(A-1) and the result is shown in Fig. 3.A-2, which shows the comparison between theoretical and experimental deformations. The experimental deformation was measured from a calibration plate inserted between the half elbows, where the plate is made of transparent thin material with 2mm interval with line-ruling of 0.3mm thick. The comparative study shows that theoretical correction reproduces well the measured deformation caused by the refractive index difference. The uncertainty interval between the theoretical and measured deformation is estimated as 3.8% of uncertainty at 95% confidence level in radial direction, while that in axial direction is negligibly small. It is noted that the deformation uncertainty in radial direction may come from the surface roughness in shaping the half elbow by milling machine.

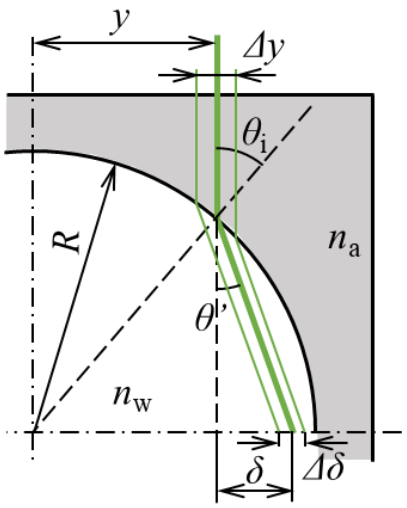

Fig. 3.A-1 Illustration of image deformation

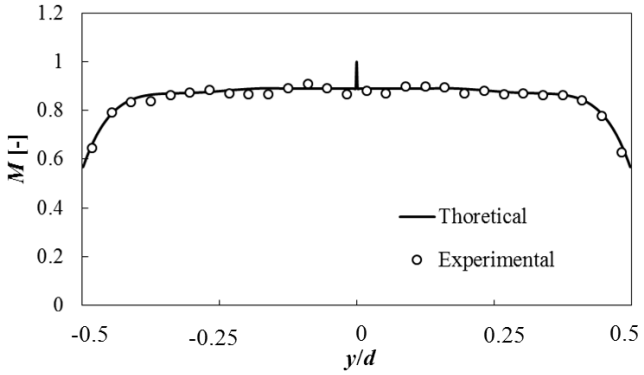

Fig. 3.A-2 Radial distribution of magnification factor

Appendix B: Mean and axial turbulence intensity contours upstream of elbow

Figs.3.B-1, 3.B-2 shows the mean velocity and the axial turbulence energy contours at upstream location of x_u/d = 2 from the elbow, respectively, which were measured by the stereo PIV system. These contour plots indicate that the flow field upstream of the elbow are almost axisymmetric. It is noted that the radial distributions of mean velocity and axial turbulence energy are plotted in Figs.3.B-1(b), 3.B-2(b), respectively, for the inlet profiles.

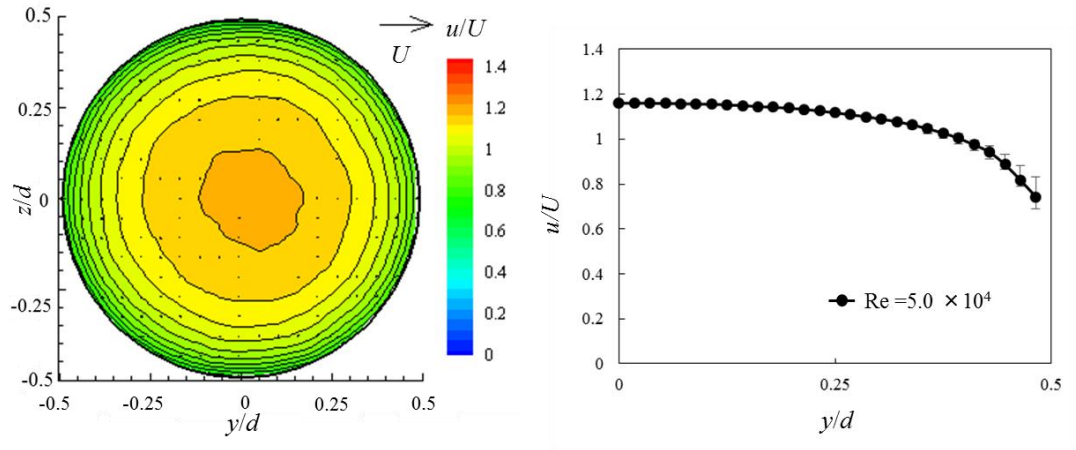

(a)Mean velocity contour (b) Radial distribution

Fig. 3.B-1 Cross-sectional mean velocity upstream of elbow

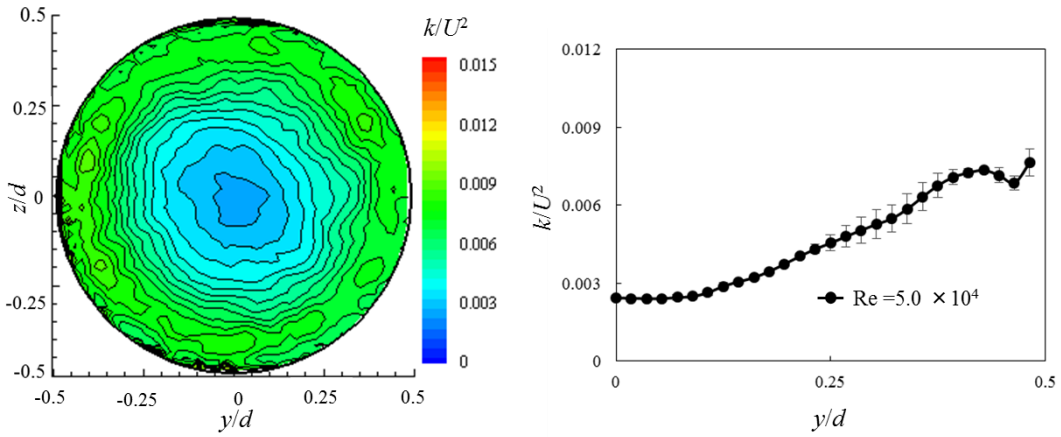

(a) Axial turbulence energy contour (b) Radial distribution

Fig. 3.B-2 Cross-sectional turbulence energy distribution upstream of elbow

References

Berkooz, G., Holmes, P., Lumley, J.L., 1993. The proper orthogonal decomposition in the analysis of turbulent flows. Annu. Rev. Fluid Mech. 25, 539–575.

Bernero, S., Fielder, H.E., 2000. Application of particle image velocimetry and proper orthogonal decomposition on the study of a jet in counterflow. Exp. Fluids. 29, S274–S281.

Fujisawa, N., Yamagata, T., Kanno, S., Ito, A., Takano, T., 2012. The mechanism of asymmetric pipe-wall thinning behind an orifice by combined effect of swirling flow and orifice bias. Nucl. Eng. Des. 252, 19-26.

Fujisawa, N., Kanatani, N., Yamagata, T., Takano, T., 2015. Mechanism of non-axisymmetric pipe-wall thinning in pipeline with elbow and orifice under influence of swirling flow, Nucl. Eng. Des. 285, 126-133.

Funatani, S., Fujisawa,N., 2002. Simultaneous measurement of temperature and three velocity components in planar cross-section by liquid crystal thermometry combined with stereoscopic particle image velocimetry. Meas. Sci. Technol. 13, 1197-1205.

Ikarashi, Y., Taguchi, S., Yamagata, T., Fujisawa, N., 2017. Mass and momentum transfer characteristics in and downstream of 90° elbow, Int. J. Heat Mass Transfer. 107, 1085-1093.

Iwamoto, Y., Minamiura, H., Sogo, M., Yamano, H., 2010. LDV measurements of a flow in a strongly-curved elbow under a high Reynolds number condition. Trans. Japan Soc. Mech. Eng. 76, 830-838. (in Japanese)

Kiuchi, M., Fujisawa, N. Tomimatsu, S., 2005. Performance of PIV system for combusting flow and its application to spray combustor model. J. Vis. 8, 269-276.

Kostas, J., Soria, J., Chong, M.S., 2005. A comparison between snapshot POD analysis

of PIV velocity and vorticity data. Exp. Fluids. 38, 146–160.

Mazhar, H., Ewing, D., Cotton, J.S., Ching, C.Y., 2016. Measurement of the flow field characteristics in single and dual S-shape 90° bends using matched refractive index PIV, Exp. Therm. Fluid Sci. 79, 65-73.

Nguyen, T., Goth N., Jones, P., Vaghetto, R., Hassan, Y., 2018. Stereoscopic PIV measurements of near-wall flow in a tightly packed rod bundle with wire spacers, Exp. Therm. Fluid Sci., 92, 420-435.

Taguchi, S., Ikarashi, Y., Yamagata, T., Fujisawa, N., Inada, F., 2018. Mass and momentum transfer characteristics in 90° elbow under high Reynolds number, Int. Comm. Heat Mass Transfer. 90, 103-110.

Wieneke, B., 2015. PIV uncertainty quantification from correlation statistics. Meas. Sci. Technol. 26, 074002.

Chapter 4

Mass transfer measurement and flow separation behavior in a 90° short elbow

4.1 Introduction

In this chapter, the mass transfer distribution in a 90° short elbow (radius to diameter ratio 1.0) were investigated experimentally in the Reynolds number range Re = (3-15)×10^4. Furthermore, the flow field near the inner wall was measured by particle image velocimetry (PIV) to understand the relation between the mass transfer distribution and the flow behavior on the inner wall of short elbow. The flow separation and the reattachment were studied in relation to the Reynolds number.

4.2. Experimental apparatus and procedures

4.2.1 Experimental set-up

The experiments on mass transfer coefficients and the separating flow behavior in the 90° elbow were carried out in a closed-circuit water tunnel, which was described in chapter 2. It consisted of a water tank with temperature controller, pump, settling chamber, straight pipe, and a test elbow, where the pipe diameter is d = 56 mm and the straight pipe length is 1,340mm (=24d). The short elbow has a radius to diameter ratio of 1.0 as illustrated in Fig. 4.1. The temperature of working fluid water was kept at 303

K and the Schmidt number was Sc (=ν/D) = 680, which is because of the plaster layer on the elbow surface in the mass transfer measurements (D: molecular diffusion coefficient). The bulk flow velocity in the major experiments was set to U=0.43, 0.72 and 1.44, which corresponds to the Reynolds numbers Re = 3×10^4, 5×10^4 and 1×10^5, respectively.

4. 2.2 Mass transfer measurement

The mass transfer measurements were carried out at five cross sections perpendicular to the elbow axis at angles α=0, 22.5, 45, 67.5, 90°, where α is defined by the angle from the elbow inlet, as shown in Fig. 4.1. To evaluate the cross sectional distribution of mass transfer coefficient on the elbow, two types of test elbows were designed: one was for the measurement on the inner and outer walls of elbow and the other was for the measurement on the side walls of elbow. The mass transfer measurements were carried out in the circumferential angle ranging from -45 to 45° (=90°) in the plane perpendicular to the elbow axis. Therefore, the whole circular distribution (=360°) of mass transfer coefficient normal to the elbow axis was evaluated by combining the results of four measurements on each half pipe section of elbow.

Mass transfer coefficients were evaluated from the measurements of the depth distribution of the plaster layer before and after the experiments in water flow (W.H.Ahmed et al. 2012, Ikarashi et al. 2017, Taguchi et al. 2018). The plaster layer casted on the wall was maintained at 3 mm thick. The surface of the plaster layer on the elbow was polished by #1000 emery paper to ensure smoothness after molding the plaster layer into the elbow. Gas bubbles generated in the liquid plaster layer were removed using the vacuum pump during the preparation of the liquid plaster.

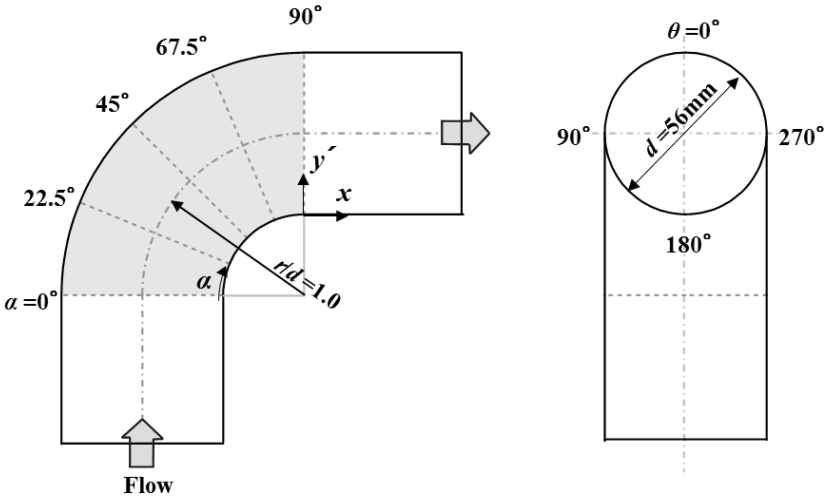

(a) Side view (b) Cross sectional view

Fig. 4.1 Illustration of 90° short elbow.

Figure 4.2 shows the experimental test section for evaluating the mass transfer coefficients on the elbow wall, which were carried out by measuring the dissolved thickness of the plaster layer into the water flow. It consisted of the traversing device driven by a stepping motor, laser displacement sensor, and the test section of half elbow on the traversing device (Chapter 2). It is noted that the wall thinning rate distribution normal to the elbow wall was evaluated from the depth distribution measurement before and after the experiments, where the correction was made on the circumferential wall angle of the elbow. The mass transfer coefficient K was obtained from the following equation;

$$K = \frac{\rho_b \delta h / \delta t}{c_w - c_b} \tag{1}$$

where $\delta h/\delta t$ is the wall-thinning rate of the plaster layer in a unit time and δh is evaluated from the depth variation of the plaster layer before and after the experiment,

ρ_b is the density of plaster layer, c_w is the concentration of the plaster layer, c_b is that of the dissolved plaster in water flow. The concentration c_w is assumed as the saturated concentration of the dissolved plaster and c_b is evaluated from the volume of dissolved plaster in the water flow. The dissolved concentration of the plaster in the bulk flow was measured by the concentration meter and was smaller than 10% of the saturated concentration of the plaster in water. The uncertainty of the mass transfer coefficient measurement was estimated to be 5.6% in the confidence level of 95%, which consists of the setting error of test elbow 10 μm in estimating the depth distribution and an error in the concentration measurement 2%, the time derivative error 1% and the minor bias error in depth measurement by laser displacement sensor 0.25% (Chapter 2). The mass transfer coefficient K was normalized by that of the straight pipe K_0. The wall surface of this experiment was considered hydraulically smooth, because the roughness height y' (=4μm) was small enough and it satisfied the condition $y'U_\tau/\nu < 1$ (U_τ: friction velocity, ν: kinematic viscosity).

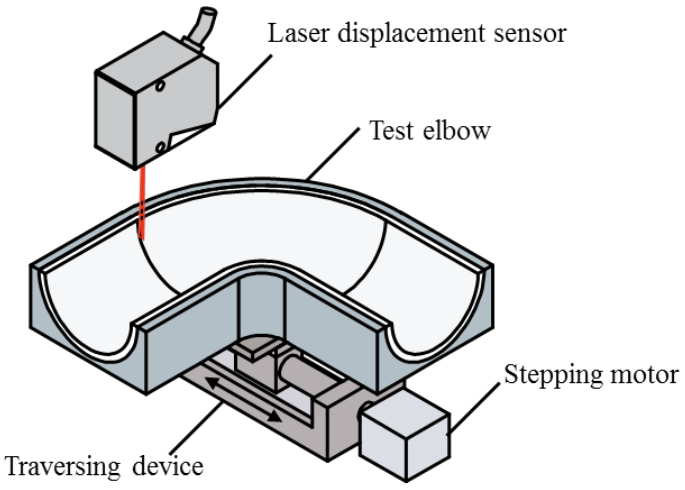

Fig. 4.2 Experimental apparatus for mass transfer measurement.

4.2.3 PIV measurement of velocity field on inner elbow wall

The instantaneous velocity field around the separated flow region on inner elbow wall was measured by PIV, which consists of the pulsed Nd:YAG laser (70mJ/pulse), CCD camera (1018 × 1008 pixels with 8 bits in gray level) and the pulse controller. The flow visualization was carried out by adding a certain amount of nylon tracer particles of 40 μm diameter with specific gravity of 1.02 to the working fluid water. The flow observation was made by a CCD camera located over the elbow model, while the light sheet illumination was provided from the side wall of the test section, as illustrated in Fig. 4.3. It is noted that the camera observation were made perpendicular to the target surface to minimize the image distortion due to refractive index difference. The thickness of the light sheet was 2 mm. Nevertheless, the near-wall velocity field was deformed by the refractive index difference at the interface of acrylic resin material and water, so that the theoretical correction was introduced into the analysis near the wall, which has been described in Ref. (Chapter 3).

The statistical properties of mean flow and fluctuating velocities were evaluated from 500 instantaneous velocity fields captured at 15 frames/s by a CCD camera in the Reynolds number range Re = (3-15) × 10^4. The observations were made in the area 60mm×60mm. The PIV analysis was carried out using the interrogation window size 31 × 31 pixels with 50% overlap, where the sub-pixel interpolation was incorporated into the analysis (Kiuchi et al. 2005). The maximum pixel displacement of the particle images was about 4 pixels in the velocity measurements by tuning the time interval between the two sequential images. As a result, the number of invalid velocity vectors was found less than 1% of the total number of velocity vectors. The uncertainty in velocity measurement was estimated to be 4.9% with respect to the maximum velocity,

while it increased near the wall owing to the increased image deformation near the acrylic resin-water interface (Chapter 3). The details of uncertainty analysis has been described in Chapter 3.

4.2.4 Evaluation of separation and reattachment points by near-wall PIV measurement

The separation and reattachment points of the separating flow on the inner wall was determined from the mean velocity profiles obtained from the near-wall PIV measurement. This experimental technique relies on the transformation of boundary-fitted coordinate image into rectangular image and the PIV analysis, which is followed by the transformation back into the velocity field in the original boundary-fitted coordinates (Oguma et al. 2007). The PIV analysis with the sub-pixel interpolation technique was carried out using the interrogation window size 41 × 21 pixels with 50% overlap because of the high-resolution requirement in vertical coordinate y' from the wall. The observation area of near-wall PIV measurement was 30mm×30mm and the nearest velocity vectors to the wall were obtained at y'=0.3mm. The separation and reattachment points were obtained from the start and end of the reverse flow at the nearest point to the wall.

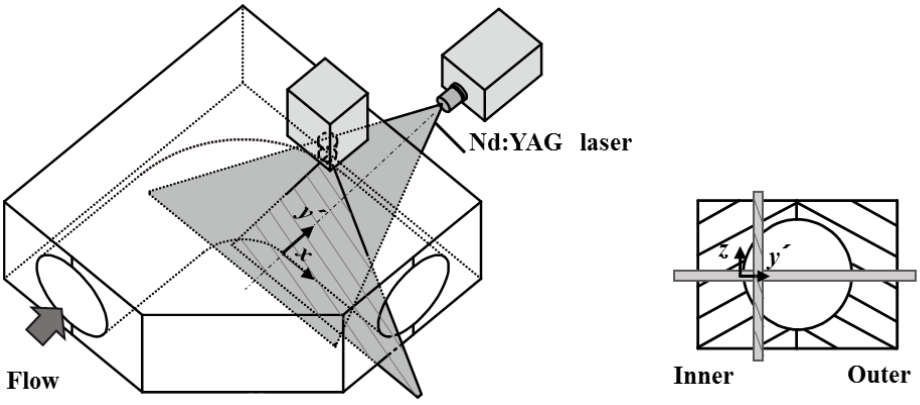

Fig. 4.3 Experimental test section for velocity measurement

4.3. Results and discussion

4.3.1 Distribution of mass transfer coefficients in short elbow

Figures 4.4(a)-(c) show the cross-sectional distributions of mass transfer coefficients in the 90° short elbow at three Reynolds numbers Re = 3×10^4, 5×10^4, 10×10^4, which are measured by the plaster dissolution method. The experimental results are averaged over ±5° in circumferential angle of the elbow obtained from three repeated experiments. The scattering of the data is shown by the error bars. It is noted that each polar graph shows the normalized mass transfer coefficient K/K_0, which are plotted against the circumferential angle θ from the outer wall of the elbow. When the normalized mass transfer coefficient K/K_0 equals to 1, the local mass transfer coefficient in the elbow is the same magnitude as that of the straight pipe. It is noted that the circumferential angle θ=0° corresponds to the outer wall, θ=180° is the inner wall and θ=90° and 270 ° are the side walls, as illustrated in Fig. 4.1(b).

Figure 4.4(a),(b) shows the distribution of normalized mass transfer coefficient at lower Reynolds number Re=3×10^4 and 5×10^4, respectively, for some elbow angles α=0°, 22.5°, 45°, 67.5°, 90°. Both results show a similar mass transfer variation with the elbow angle α. The normalized mass transfer coefficient is almost equal to 1 at the inlet of the elbow α=0°, while it shows a large variation in magnitude with increasing the elbow angles α on the inner wall, which is apparent at the end of elbow (α=90°). Detail examination on the mass transfer distribution shows that K/K_0 on the inner wall decreases at α=22.5° (Fig. 4.4(a),(b)) with respect to that on the elbow inlet (α=0°), while it increases on the side walls. This is similarly observed on the elbow angle α=45° but it shows a local minimum ±20° on both sides of the elbow centerline. This variation of mass transfer coefficient with the elbow angle may be related to the start of high

velocity converging flow outside the separating flow region on the inner wall of the elbow, which will be shown in Fig. 4.12. With further increases in the elbow angle to α=67.5° and 90°, the mass transfer coefficient on the side wall keeps roughly the same magnitude as that of α=45°, but the significant increase is observed on both sides of the inner wall at θ= ±25° (double peaks), where the mass transfer coefficient reaches almost 2 times in magnitude of the smooth pipe. This was not observed in the long elbow, so that it can be one of the features of short elbow.

When the Reynolds number of the flow through the elbow increases to Re=1 × 10^5, the mass transfer coefficient distribution changes drastically due to the influence of Reynolds number. The mass transfer coefficient decreases on the inner wall of the elbow and it increases on the inner side walls (α=67.5° and 90°), which results in the disappearance of the double peaks on the mass transfer distribution and results in a more uniform mass transfer coefficient distribution on the inner wall of the elbow. Therefore, the mass transfer distribution on the whole elbow at higher Reynolds number Re=1 × 10^5 behaves differently from that on the lower Reynolds number flows (Re=(3-5) × 10^4). It is seen that the double peaks are suppressed on both sides of the elbow centerline, but the mass transfer coefficient in the elbow centerline stays in a high magnitude. This may be caused by the influence of Reynolds number on the flow field on the inner wall, which appears in the separated flow region on the second half of the inner wall, which will be shown in Fig. 4.5. On the other hand, the mass transfer coefficient on the outer elbow wall slightly decreases at higher Reynolds number (Re= 1 × 10^5), which results in the mass transfer coefficient lower than the straight pipe. This may be due to the flow acceleration effect on the outer elbow wall with increasing the Reynolds number.

Figure 4.4(d) shows the comparative study of mass transfer coefficient distribution at α=90° of short elbow (*r*/*d*=1.0) and long elbow (*r*/*d*=1.5) at two Reynolds numbers Re=5 × 10^4 and 1 × 10^5, which are the typical examples of low and high Reynolds numbers. These results indicate that the major difference of mass transfer distribution at low Reynolds number arises on the inner wall at low Reynolds number, which is the double peaks on the short elbow on both sides of the centerline, while the single peak was observed on the long elbow around the centerline. When the Reynolds number is increased to Re=1 × 10^5, both the double peaks and single peak of mass transfer distribution is decreased on the inner elbow wall and that of the neighboring side wall increased, which results in a uniform mass transfer distribution on the inner elbow wall in circumferential direction. A decrease in the mass transfer distribution is observed on the outer elbow wall on short and long elbows.

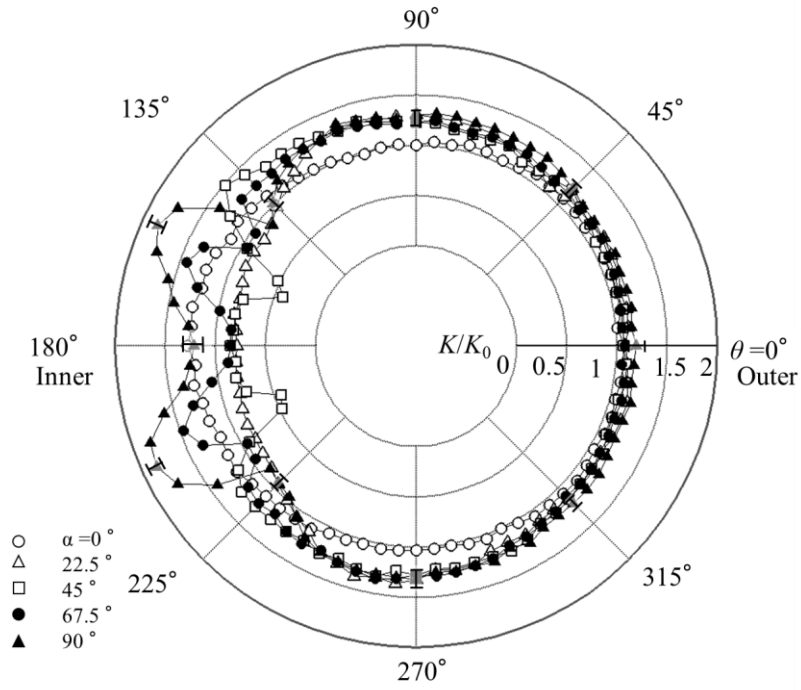

(a)Re =3×10^4

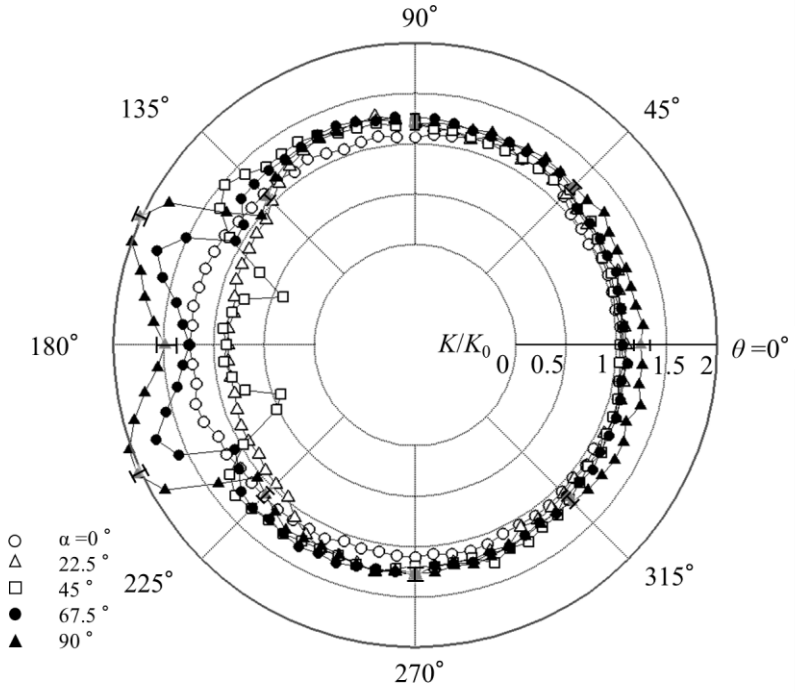

(b) Re =5×10^4

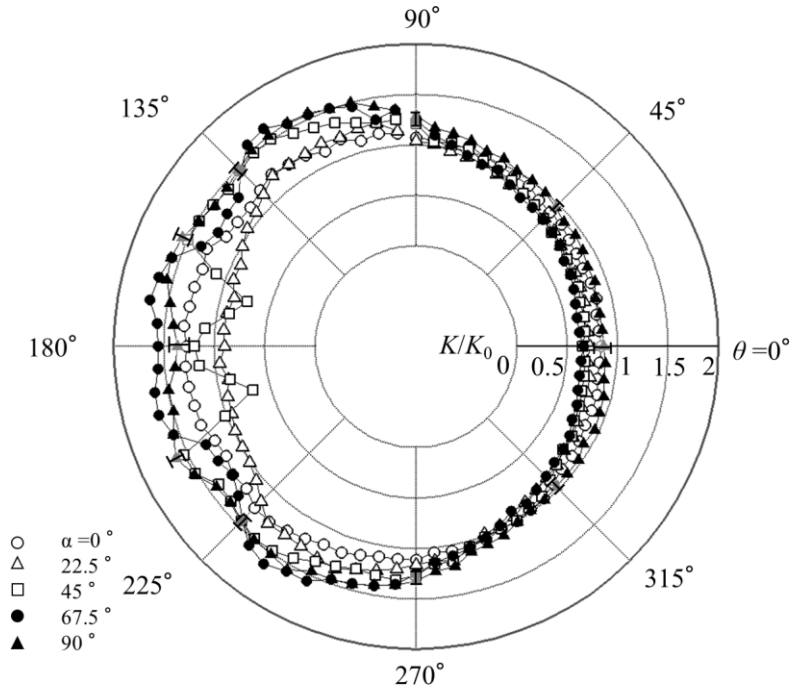

(c)Re =1×10^5

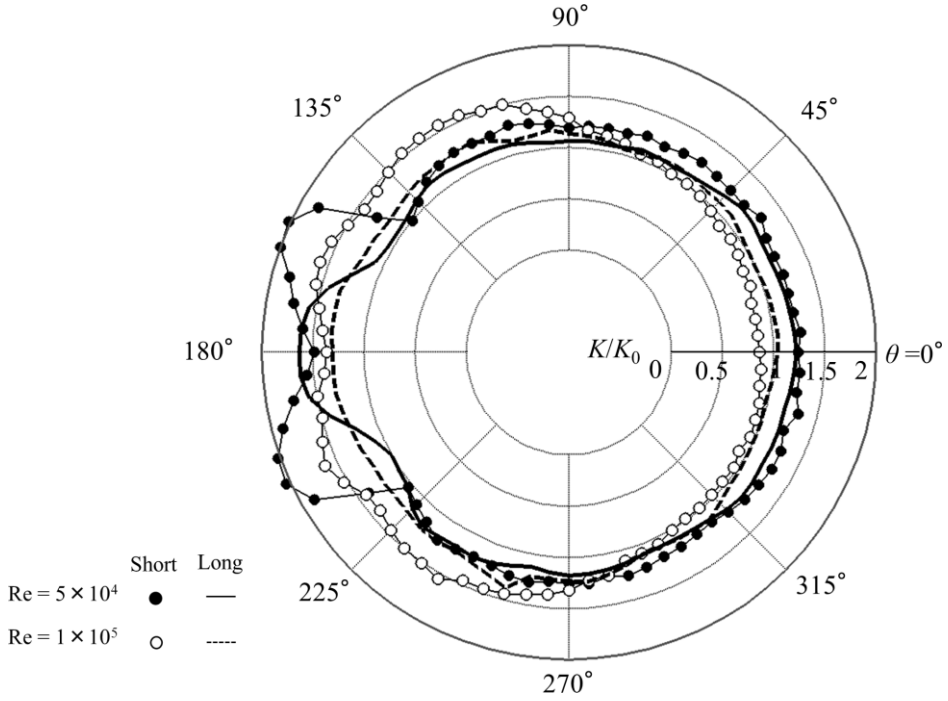

(d) Comparison with long elbow (α=90°)

Fig. 4.4 Cross-sectional mass transfer distributions in short elbow

4.3.2 PIV measurement of velocity field over separating flow region

To characterize the separating flow behavior on the inner wall of the elbow, the velocity field on the second half of the inner wall of the elbow was measured by a planar PIV at some Reynolds numbers Re = (3-15)×10^4. Figs. 4.5(a),(b),(c) shows the axial cross-section of mean velocity distributions of the flow in the second half of the elbow and downstream at three Reynolds numbers Re=3×10^4, 5×10^4, 1×10^5, respectively. The mean velocity contour at Re=3×10^4 (a) shows a clear indication of flow separation on the second half of the elbow and it prevails over the downstream region of the elbow. The separating flow region ends by the attachment, which occurs at x/d=0.5 on the downstream of the elbow. With an increase in the Reynolds number to Re=5×10^4, the separation point is almost the same as the lower Reynolds number case, but the reattachment point moves upstream, resulting in a decrease in the axial length of

separating flow region. With further increase in Reynolds number to $Re=1\times10^5$, the separating flow region becomes much smaller than that of the low Reynolds number case, but the lower velocity region still remains in the downstream of the elbow. The detailed examination of the mean velocity over the inner elbow wall and downstream can be performed in the mean velocity profiles in Fig. 4.6, which shows the near-wall velocity distribution more clearly. The results indicate that the delay of flow separation on the inner wall with increasing the Reynolds number and the subsequent recovery of the mean velocity in the downstream of the elbow.

Fig. 4.7(a),(b),(c) shows the axial turbulence intensity contour in the second half of the elbow and downstream at three Reynolds numbers $Re=3\times10^4$, 5×10^4, 1×10^5, respectively. The turbulence intensity increases near the separation points and develops along the shear layer, which results in the formation of high turbulence intensity region in the downstream of the elbow. With increasing the Reynolds number, the magnitude of axial turbulence intensity increases along the shear layer but the highly turbulent region is suppressed because of the decrease in the separating flow region on the inner wall of the elbow in Fig. 4.5. It is noted that the suppression of high turbulence intensity region at higher Reynolds number is closely related to the decrease in the separating flow region downstream of the elbow.

The detailed examination of axial turbulence intensity profiles in and downstream of short elbow are shown in Fig. 4.8. These results indicate that the maximum axial turbulence intensity is located near the wall at higher Reynolds number, which is caused by the downstream movement of the separation point. This results in the higher axial turbulence intensity near the wall and lower intensity in the far region of the inner wall

at higher Reynolds number. The turbulence intensity profile recovers downstream of the elbow independent of the reattachment points.

To clarify the Reynolds number effect on the separating flow region, the near-wall mean velocity profiles are measured by the near-wall PIV. This is because of the high spatial resolution requirement of the near-wall velocity to obtain the separation and reattachment points. An example of mean velocity profiles near the separation point is shown in Fig. 4.9 at Re = 3×10^4, 5×10^4, 1×10^5. The result shows that the flow separation occurs at the angle α=38° (Re = 3×10^4), α=42° (Re = 5×10^4), α=48° (Re = 1×10^5), which are the start of reverse flow in the near-wall velocity profiles.

The separation and reattachment points obtained from the near-wall PIV measurement are summarized in Fig. 4.10 with respect to the Reynolds number. The results indicate that the separation point behaves weakly dependent of the Reynolds number and it moves slightly downstream with increasing the Reynolds number. On the other hand, the reattachment point moves upstream with increasing the Reynolds number, which is highly observed in the low Reynolds number. Therefore, the axial length of separating flow region, which corresponds to the axial distance between the separation and reattachment points, decreases with increasing the Reynolds number. The variation of the axial length of the separating flow region seems to be saturated at higher Reynolds numbers Re= (1 - 1.5)$\times10^5$. The uncertainties in separation and reattachment points are shown by error bars in Fig. 4.10, which are obtained from the repeated experiments.

Figure 4.11 shows the mean velocity distribution over the inner wall of the elbow and downstream in the cross-sectional plane parallel to the inner wall at three Reynolds numbers Re=3×10^4, 5×10^4, 1×10^5, respectively. The light-sheet plane from the inner

wall was set to y'=4mm. The results indicate that the separating flow region is formed in the mid plane down to x/d=0.5 at lower Reynolds number Re=3×10^4. With an increase in Reynolds number, the separation region decreases mainly due to the reattachment point movement and it is almost diminished at higher Reynolds number Re=1×10^5. These results agree with the observation of reattachment points in Fig. 4.10. This figure also shows the circumferential distribution of separating flow region, which extends to z/d=±0.07, which corresponds to almost ±8° on the inner wall of the elbow. The mean velocity distribution around the separating flow region indicates the formation of conversing flow in the downstream of the separating flow region, which shows a local maximum velocity on both sides of the elbow centerline z/d=±0.19 (22°). It should be mentioned that the velocity gradient in z direction gradually decreases with increasing the Reynolds number because of the suppression of separating flow region.

Figure 4.12 shows the corresponding axial turbulence intensity contours in the cross sectional plane parallel to the inner wall at three Reynolds numbers Re=3×10^4, 5×10^4, 1×10^5, respectively, with a distance y'=4mm from the inner wall. The turbulence intensity contour at Re=3×10^4 shows the high turbulence intensity on both sides of the elbow centerline, which corresponds to the outer shear layer surrounding the separating region z/d=±0.16 (19°). It should be mentioned that the high turbulence intensity region is located in the middle of the shear layer with high velocity gradient and it is slightly closer to the elbow centerline than the position of maximum velocity. With increasing the Reynolds number to Re=5×10^4, the high turbulence intensity region comes closer to the elbow centerline and they almost merge together at higher Reynolds number Re=1×10^5. It should be mentioned that the location of the maximum turbulence intensity z/d=±0.16 (19°) agrees with that of the double peak positions (20°) in the mass

transfer distribution in Fig. 4.4. This suggests that the double peaks in mass transfer distribution may be caused by the local high turbulence. Furthermore, the Reynolds number effect on the maximum turbulence intensity position is similarly observed in the behavior of double peak positions in the mass transfer coefficient, which comes closer to the elbow centerline with increasing the Reynolds number. Therefore, the high mass transfer coefficient on the inner wall of the elbow is considered to be caused by the high turbulence intensity on the inner wall, which is caused by the high velocity gradient of the converging shear layer on both sides of the elbow centerline.

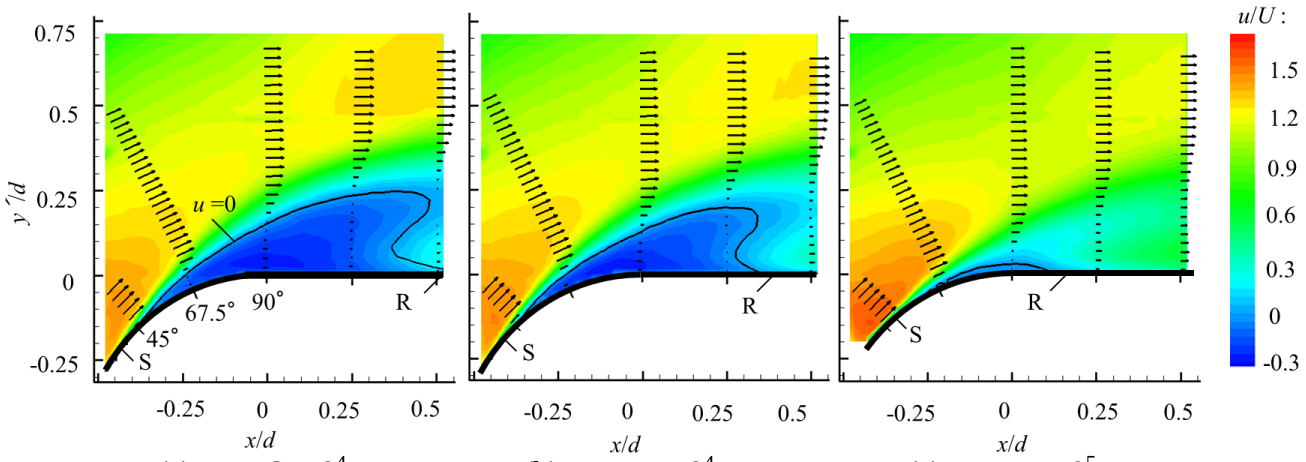

(a) Re = 3×10^4 (b) Re = 5×10^4 (c) Re = 1×10^5

Fig. 4.5 Mean velocity contours in and downstream of short elbow

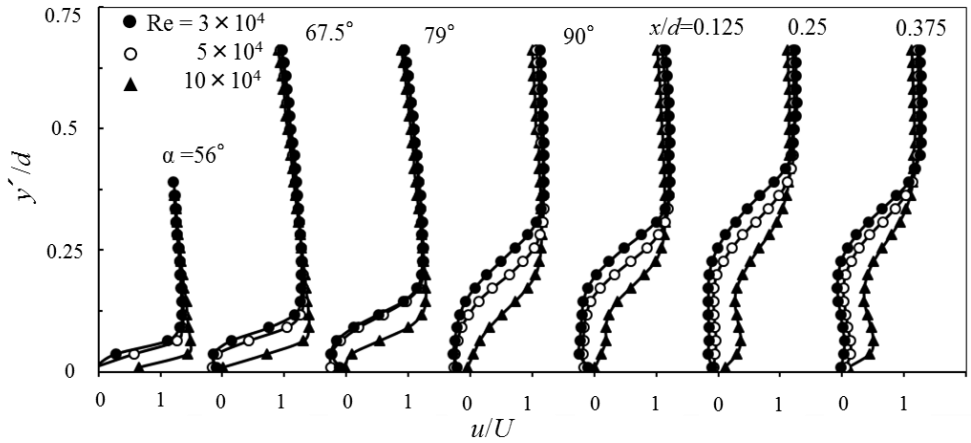

Fig. 4.6 Mean velocity distribution in and downstream of short elbow

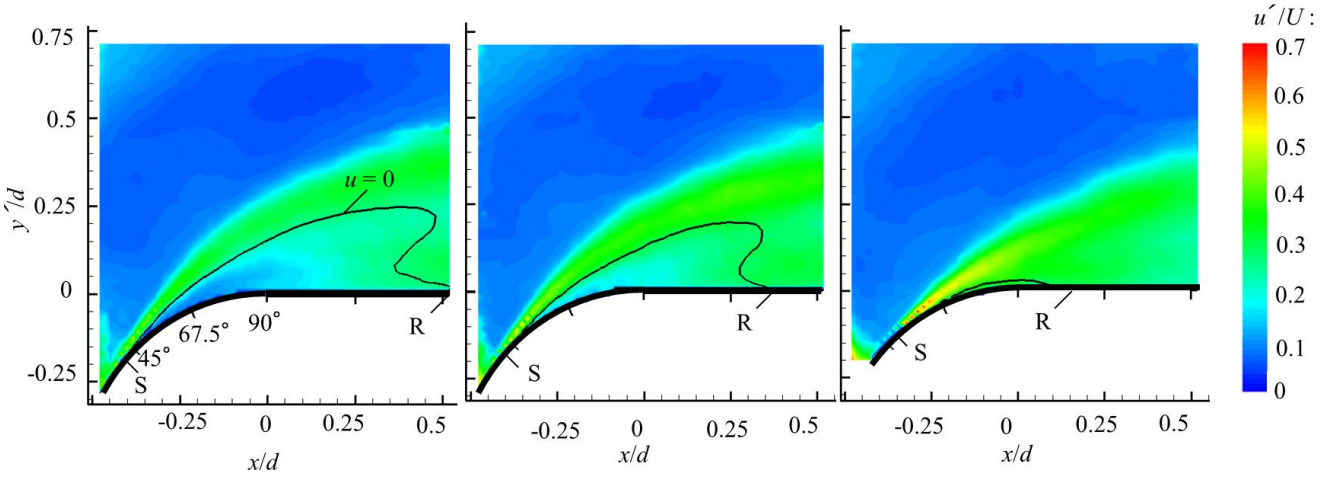

(a) Re = 3×10^4 (b) Re = 5×10^4 (c) Re = 1×10^5

Fig. 4.7 Axial turbulence intensity contour in and downstream of short elbow

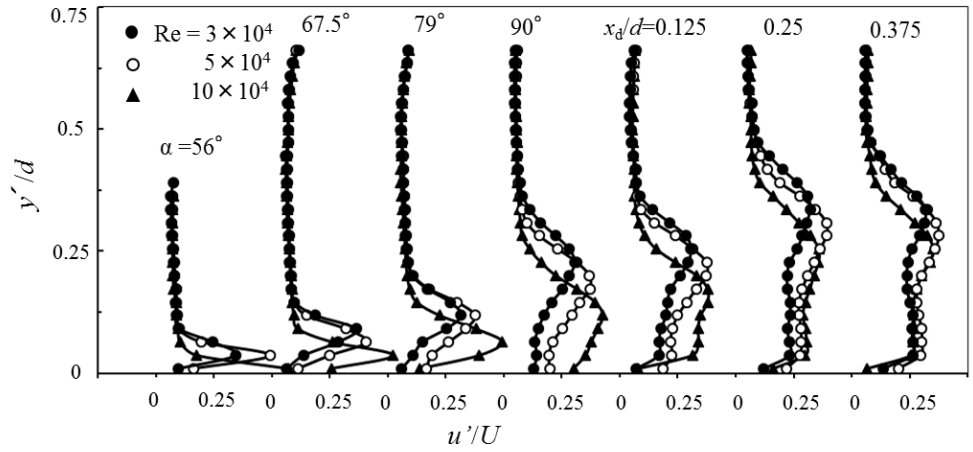

Fig. 4.8 Axial turbulence intensity distributions in and downstream of short elbow

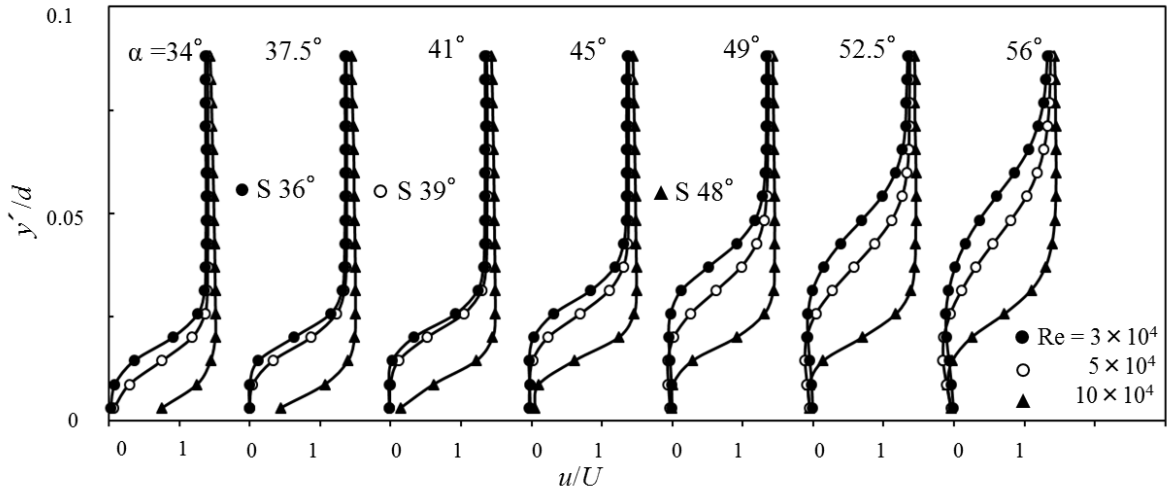

Fig. 4.9 Example of mean velocity profile near separation point

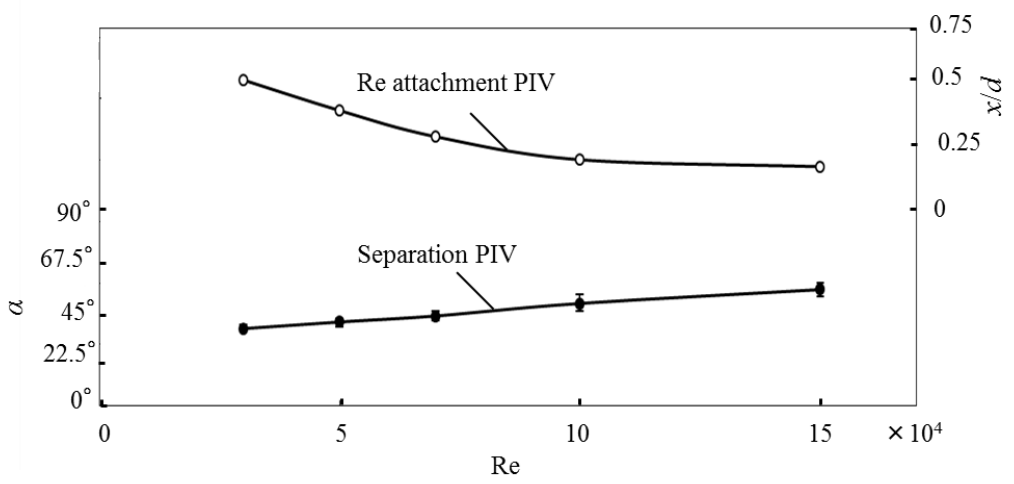

Fig. 4.10 Downstream variation of separating flow region in and downstream of short elbow

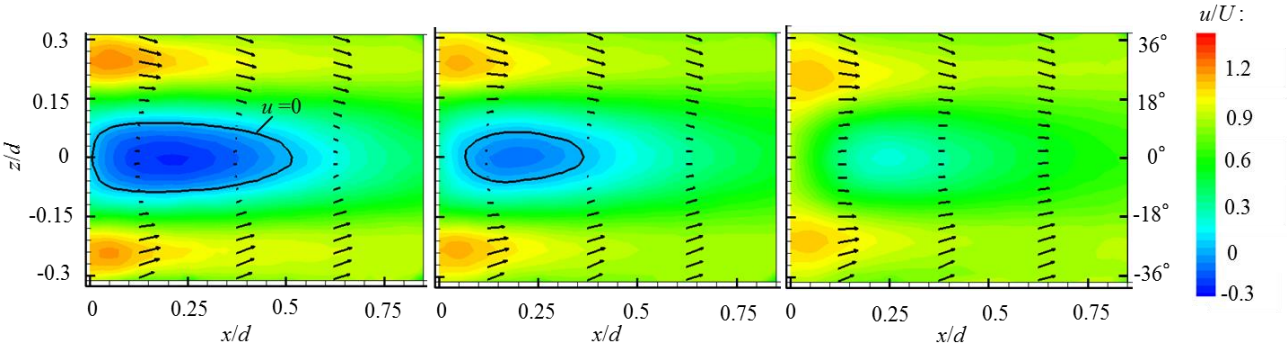

(a) Re = 3×10^4 (b) Re = 5×10^4 (c) Re = 1×10^5

Fig. 4.11 Near-wall mean velocity contour in horizontal cross section

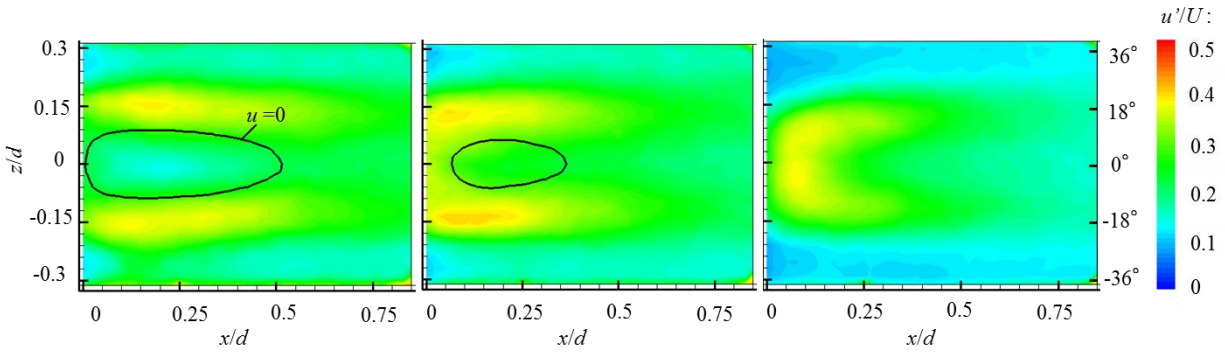

(a) Re = 3×10^4 (b) Re = 5×10^4 (c) Re = 1×10^5

Fig. 4.12 Near-wall axial turbulence intensity contour in horizontal cross section

4.4. Conclusion

Mass transfer coefficient distribution and flow separation behavior in a 90° short elbow with a radius to pipe diameter ratio of 1.0 were studied experimentally using the plaster dissolution method and PIV measurements in a Reynolds number range Re = (3-15)×10^4. The influence of Reynolds number on the mass transfer coefficient distribution is only weakly observed in the first half of the inner elbow wall, while it is a large change in the second half of the inner wall, which is the generation of high mass transfer region on both sides of the elbow centerline on the inner wall. To understand this phenomenon, PIV measurements were carried out on the inner elbow wall and

observed the flow separation and reattachment in the second half of the elbow. It was found that the high mass transfer characteristics on the inner wall of the second half of the elbow is highly correlated with the separating flow behavior in and downstream of the short elbow. With increasing the Reynolds number, separation point moves downstream and the reattachment point moves upstream, which results in the suppression of separation region with increasing the Reynolds number. Furthermore, the circumferential extent of the separation region decreases with increasing the Reynolds number, which arises from the shift of converging flow on both sides of the separating flow region. Thus, the high turbulence intensity region comes closer to the elbow centerline with increasing the Reynolds number. The variation of high turbulence intensity region on both sides of the centerline with the Reynolds number is consistent with that of the high mass transfer region. Therefore, the high mass transfer behavior in the 90° short elbow arises from the generation of separating flow region and the behavior of turbulent flow over the inner wall of the elbow.

References

Berger F.P., Hau K.F.F.L., Mass transfer in turbulent pipe flow measured by the electrochemical method, Int. J. Heat Mass Transfer, 20 (1977), 1185-1194.

Yoneda K., Morita R., Investigation of the flow in orifice downstream affecting flow accelerated corrosion, Proc. 15th Int. Conf. Nucl. Eng., Nagoya, 2007, 10200.

Kim K.H., Park S.H., Hwang K.M., Verification of the interrelation between local wall thinning and velocity components observed in the deflected turbulent flow inside orifice of carbon steel piping, Microsyst. Technol. 16(2010) 1945-1950.

Ohkubo M., Kanno S., Yamagata T., Takano T., Fujisawa N., Occurrence of asymmetrical flow pattern behind an orifice in a circular pipe, J. Vis. 14(2011), 15-17.

Xiong J., Koshizuka S., Sakai M., Turbulence modelling for mass transfer enhancement by separation and reattachment with two-equation eddy viscosity models. Nucl. E,ng. Des. 241(2011), 3190-3200.

El-Gammal M., Ahmed W.H., Ching C.Y., Investigation of wall mass transfer characteristics downstream of an orifice, Nucl. Eng. Des. 242 (2012) 353-360.

Shan F., Fujishiro A., Tsuneyoshi T., Tsuji Y., Particle image velocimetry measurements of flow field behind a circular square-edged orifice in a round pipe, Exp. Fluids 54 (2013), 1553.

Takano T., Ikarashi Y., Uchiyarna K., Yamagata T., Fujisawa N., Influence of swirling flow on mass and momentum transfer downstream of a pipe with elbow and orifice, Int. J. Heat Mass Transfer, 91 (2016), 394-402.

Spedding, P.L. Benard E., McNally G.M., Fluid flow through 90 degree bends, Dev. Chem. Eng., Mineral Process, 12 (2004), 107-128.

Crawford N.M., Cunningham G., Spence S.W.T., An experimental investigation into the pressure drop for turbulent flow in 90° elbow bends, Proc. IMech E, 221 (2007), 77-88.

Ono A., Tanaka M., Kobayashi J., Kamide H., Influence of inlet velocity condition on unsteady flow characteristics in piping with a short elbow under a high-Reynolds-number condition, Mech. Eng. Journal, 4(2017), Paper No.16-00217.

Ikarashi Y., Uno T., Yamagata T., Fujisawa N., Influence of elbow curvature on flow and turbulence structure through a 90° elbow, Nucl. Eng. Des. (2018), pp. 181-193.

Oguma Y., Fujisawa N., Near-wall velocity measurement over an airfoil by PIV, J. Vis 10 (2007), 157-158.

Chapter 5

Concluding Remarks

In this thesis, the mass and momentum transfer in a 90 elbow was experimentally studied to clarify the mechanism of pipe-wall thinning of pipeline in power plant. The results can be summarized as follows.

(1) The mass transfer characteristics of a 90° long elbow were measured by plaster dissolution method and the results were examined combining with the surface flow visualization and the PIV measurements of velocity field. These experimental results indicate that the lower mass transfer coefficients are generated in the first half of the inner wall and it increases in the second half of the inner wall. Furthermore, the variations of mass transfer coefficient in the elbow were found to be highly correlated with the surface flow pattern observed by the surface flow visualization. The PIV measurements of velocity field shows the growth of turbulence energy in the second half of the inner wall, which is due to the combined influence of flow convergence and separation in the elbow.

(2) The influence of elbow radius ratio and the Reynolds number on the velocity fields in and downstream of a 90° elbow were studied experimentally using PIV measurements. The results indicate that the axial mean velocity decreased along the inner wall in the second half of the elbow and the flow approached separation near the outlet of the inner wall. The turbulence intensity and Reynolds stress increased along the inner wall, and the secondary flow was highly promoted in the elbow outlet. These effects of the radius ratio were highly promoted in the short elbow, where flow separation occurred near the elbow outlet. The in-plane velocity measurements in the cross-sectional plane of the elbow outlet indicated the presence

of a pair of counter-rotating vortices. The velocity magnitude and turbulence energy increased with decreasing radius ratio of the elbow.

(3) The POD analysis indicated that the counter-rotating vortices is generated in and downstream of the elbow, which is generated across the cross section of the pipe from the inner wall to the outer wall. The vortices promoted the secondary flow in the cross-section of the elbow and resulted in a growth of turbulence energy on the inner wall with decreasing radius ratio. This result indicates the growth of mass transfer enhancement on the second half of the inner wall of the elbow.

(4) The measurements of mass and momentum transfer characteristics in a 90° short elbow indicate that the mass transfer is highly magnified on the second half of the inner wall. With decreasing the radius to diameter ratio of the elbow, the mass transfer coefficient increases on the second half of the inner wall caused by the flow separation in and downstream of the short elbow. It is also found that the mass transfer coefficient on the inner wall decreases with increasing the Reynolds number, which is caused by the suppression of flow separation on the inner wall at high Reynolds number. This suggests an increase of pipe-wall thinning on the inner wall of the short elbow, but it can be decreased with increasing the Reynolds number.

Acknowledgements

The author would like to express gratitude towards my supervisor of Professor Nobuyuki Fujisawa of Niigata University for the helpful suggestions on this research. This work was financially supported by JSPS KAKENHI Grant Numbers JP24360391, JP18K04632.

The author also thank to Professor Shin-ichi. Akabayashi, Professor Takatsune Narumi, Professor Koji Matsubara, and for the advice about this research. The helpful suggestions are acknowledged, Dr. Takayuki Yamagata of Niigata University, Dr. Fumio Inada, and Dr. Kazutoshi Fujiwara from Central Research Institute of Electric Power Industry. I would like to thank Takuji Haneda and Misao Takasaki technical staff of laboratory, and would also like to thank Shoichi Taguchi, and Fuminori Yamagisi, Yoshiki Kaneko, and Taku Uno.

I would like to thank my parents for supporting me during the course of my study.